

# X-ray Study of the Intermediate-Mass Young Stars Herbig Ae/Be Stars

Kenji Hamaguchi<sup>1</sup>

*Laboratory for High Energy Astrophysics, NASA/Goddard Space Flight Center, Greenbelt,  
MD 20771, USA*

[kenji@milkkyway.gsfc.nasa.gov](mailto:kenji@milkkyway.gsfc.nasa.gov)

Shigeo Yamauchi

*Faculty of Humanities and Social Sciences, Iwate University, 3-18-34 Ueda, Morioka, Iwate  
020-8550, Japan*

[yamauchi@iwate-u.ac.jp](mailto:yamauchi@iwate-u.ac.jp)

and

Katsuji Koyama

*Department of Physics, Faculty of Science, Kyoto University  
Kitashirakawa-oiwakecho, Sakyo, Kyoto 606-8502, Japan*

[koyama@cr.scphys.kyoto-u.ac.jp](mailto:koyama@cr.scphys.kyoto-u.ac.jp)

## ABSTRACT

We present the *ASCA* results of intermediate-mass pre-main-sequence stars (PMSs), or Herbig Ae/Be stars (HAeBes). Among the 35 *ASCA* pointed-sources, we detect 11 plausible X-ray counterparts. X-ray luminosities of the detected sources in the 0.5–10 keV band are in the range of  $\log L_X \sim 30$ –32 ergs s<sup>−1</sup>, which is systematically higher than those of low-mass PMSs. This fact suggests that the contribution of a possible low-mass companion is not large. Most of the bright sources show significant time variation, particularly, two HAeBes - MWC 297 and TY CrA - exhibit flare-like events with long decay timescales (*e*-folding time  $\sim 10$ –60 ksec). These flare shapes are similar to those of low-mass PMSs. The X-ray spectra are successfully reproduced by an absorbed one or

---

<sup>1</sup>National Research Council, 500 Fifth Street, NW, Washington, DC 20001, USA

two-temperature thin-thermal plasma model. The temperatures are in the range of  $kT \sim 1\text{--}5$  keV, which are significantly higher than those of main-sequence OB stars ( $kT < 1$  keV). These X-ray properties are not explained by wind driven shocks, but are more likely due to magnetic activity. On the other hand, the plasma temperature rises as absorption column density increases, or as HAeBes ascend to earlier phases. The X-ray luminosity reduces after stellar age of a few  $\times 10^6$  years. X-ray activity may be related to stellar evolution. The age of the activity decay is apparently near the termination of jet or outflow activity. We thus hypothesize that magnetic activity originates from the interaction of the large scale magnetic fields coupled to the circumstellar disk. We also discuss differences in X-ray properties between HAeBes and main-sequence OB stars.

*Subject headings:* radiation mechanisms: thermal, stars: early-type, stars: evolution, stars: magnetic fields, stars: pre-main sequence, X-rays: stars

## 1. Introduction

Main sequence stars (MSs) in the intermediate-mass range ( $2\text{--}10 M_\odot$ ) exhibit no significant X-ray activity (e.g. Rosner et al. 1985; Berghöfer et al. 1997), due to the absence of X-ray production mechanisms: neither strong UV field to accelerate high-speed stellar winds working in high-mass stars, nor surface convection responsible for magnetic activity working in low-mass stars. Intermediate and high-mass stars in the pre-main-sequence (PMS) stage, called Herbig Ae/Be stars (HAeBes, Herbig 1960; Waters & Waelkens 1998) have also neither strong UV fields nor surface convection zones, hence no X-ray emission is predicted for them. Nevertheless the *ROSAT* and *Einstein* surveys detected the X-ray emission from significant numbers of HAeBes (Zinnecker & Preibisch 1994; Damiani et al. 1994). Damiani et al. (1994), using *Einstein*, detected X-ray emission from 11 HAeBes out of 31 samples. They found that Be stars are more luminous than Ae stars, and suggested that the X-ray luminosity correlates to the terminal wind velocity, but not to the stellar rotational velocity  $v_{\text{rot}} \sin i$ . Zinnecker & Preibisch (1994) detected 11 HAeBes out of 21 *ROSAT* samples. In contrast to the *Einstein* result, they found no significant difference of X-ray luminosity between Be and Ae stars. They found no correlation of X-ray luminosity to  $v_{\text{rot}} \sin i$ , but found a correlation to mass loss rate. Thus both the *ROSAT* and *Einstein* results suggested that X-ray emission of HAeBes relates to the stellar winds.

The *ASCA* spectra from some bright HAeBes (HD 104237, IRAS 12496–7650 and MWC 297) exhibited high temperature plasma ( $kT \sim 3$  keV), while MWC 297 exhibited a large X-ray flare (Skinner & Yamauchi 1996; Yamauchi et al. 1998; Hamaguchi et al. 2000).

Such hot plasma and/or rapid X-ray variability can not be produced by stellar wind. Such properties are usually seen in low-mass stellar X-rays originating from magnetic activity. In fact, magnetic activity of HAeBes may be found in the powerful outflows and jets (Mundt & Ray 1994).

Wide band imaging spectroscopy between 0.5–10 keV first enabled with *ASCA* is a powerful tool to measure plasma temperatures and time variations. We thus perform a survey of HAeBes using the *ASCA* archive. From the systematic X-ray spectrum and timing analysis, we study the origin of the X-ray emission from HAeBes with reference to the *ROSAT* and *Einstein* results. The combined analysis leads us to an overall picture across the whole pre-main-sequence (PMS) phase of low and intermediate-mass stars.

This paper comprises as follows. The method of target selection is described in Section 2. Data analysis and brief results are summarized in Section 3. Comments on individual sources are in Section 4. The discussion of the X-ray emission mechanism and related phenomena to MS stars are described in Section 5 and 6. Section 7 summarizes results.

## 2. Target Selection & Data Reduction

We obtained X-ray data from 6 HAeBes, V892 Tau, IRAS 12496–7650, MWC 297, HD 176386, TY CrA, and MWC 1080 with our *ASCA* guest observing programs. We further picked up HAeBe samples from the *ASCA* archive using the comprehensive catalog compiled by Thé et al. (1994) (above spectral type F in Table i, ii and v) and the recent lists by van den Ancker et al. (1997, 1998). We also analyzed the proto-HAeBe EC95 (Preibisch 1999), that is not included in the statistical analysis of HAeBe X-ray properties but used for evolutional study of the X-ray emission. The list of the observed HAeBes is given in Table 1. Optical positions in Column 2, 3 and distance in Column 4 are from *HIPPARCOS* if available (van den Ancker et al. 1997, 1998; Bertout et al. 1999). The *ASCA* observation log is shown in Table 2.

The fourth Japanese X-ray satellite *ASCA*, launched in 1993, has four multi-nested Wolter type I X-ray telescopes (XRT), on whose focal planes two X-ray CCD cameras (Solid-state Imaging Spectrometer: SIS) and two gas scintillation proportional counters (Gas Imaging Spectrometer: GIS) are installed (Tanaka et al. 1994). The XRTs have a cusped shape point spread function (*psf*) with the half power diameter of  $\sim 3'$ , which is slightly degraded for the GISs by their detector response. The effective area of the four sets of mirrors are around  $1400 \text{ cm}^{-2}$  at 2 keV and  $900 \text{ cm}^{-2}$  at 5 keV. Bandpasses of the SIS and the GIS combined with the XRT are around 0.4–10 keV and 0.7–10 keV, respectively. The SISs

have moderate spectral resolution of  $\sim 130$  eV at 5.9 keV and field of view (*fov*) of  $20' \times 20'$  with four CCD chips fabricated on each SIS (Burke et al. 1994; Yamashita et al. 1999). A CCD chip needs 4 seconds to be read out, and runs of 1, 2 and 4 chips (corresponding to 1, 2 and 4 CCD modes) need 4, 8 and 16 seconds in an exposure, respectively. After  $\sim 1995$ , spectral resolution of data taken with 2 and 4 CCD modes significantly degraded, which is caused by development of pixel-to-pixel variation of dark current (residual dark distribution: RDD). The clocking and telemetry modes of the SIS detectors are summarized in Column 5. The GISs have energy resolution of  $\sim 460$  eV at 5.9 keV and wide *fov* (50' diameter) (Ohashi et al. 1996; Makishima et al. 1996). All observations except for PSR J0631 were made with the standard GIS (PH) mode, while a non-standard bit assignment (9-8-8-0-0-0-7) was used for PSR J0631.

We use the *ASCA* "revision2" archival data. The data basically do not need further reduction, but the degradation of the SIS data by RDD in the 2 and 4 CCD modes are restored using *correctrdd* (Dotani et al. 1997). We remove hot and flickering pixels in the SIS using *sisclean* and select the *ASCA* grade 0234. The GIS events are selected using *gisclean* (Ohashi et al. 1996). Both the SIS and the GIS data are screened using the standard criteria, which excludes data in the South Atlantic Anomaly, Earth occultation and high-background regions with low-geomagnetic rigidities. The SIS data with viewing angle less than  $20^\circ$  above the day-earth horizon are also excluded. Analyses are made using the software package FTOOLS 4.2, XIMAGE ver. 2.53, XSPEC ver. 9.0 and XRONOS ver. 4.02.

### 3. Analysis & Results

#### 3.1. Source Detection

The analysis is basically made in the 0.5–10 keV band for the SIS and the 0.8–10 keV band for the GIS. The low energy threshold for the SIS is set at slightly higher level than those of the onboard discrimination because the low energy efficiency at these levels are degraded by RDD and the event splitting effects can not be fully corrected by *correctrdd*.

We made X-ray images for both the SIS and the GIS in J2000 coordinate, where the absolute coordinate is corrected by the method in Gotthelf et al. (2000). The positional accuracy for the SIS bright sources should be within  $\sim 12''$ . We searched for X-ray sources above  $5\sigma$  detection level around the position of relevant HAeBe. Still possible mis-identification to nearby sources can not be excluded in crowded regions. We checked the *ROSAT* results in Zinnecker & Preibisch (1994) and Preibisch (1998) and/or retrieved the *ROSAT* images (Table 3) to confirm the source identifications. To extract the X-ray events for spectral and

timing analysis, we normally took a circle of  $2.5'$  or  $3'$  radius around the relevant source. The background region is selected from the nearby source-free region or at the symmetrical region with respect to a contaminating source, if any. The selected background regions are summarized in Table 4.

For non-detected HAeBes, we determine the  $3\sigma$  upper-limit (99% confidence levels) from a  $40''$  square region for the SIS and a  $80''$  square region for the GIS. The background data are taken from a nearby source-free region with the *sosta* package in XIMAGE. The upper-limits are converted to fluxes using the PIMMS package assuming an absorbed thin-thermal model with  $kT = 1$  keV, abundance =  $0.3 Z_{\odot}$  and  $N_{\text{H}}$  converted from  $Av$  ( $N_{\text{H}} \sim 2.2 \times 10^{21} Av \text{ cm}^{-2}$ , Ryter 1996). The upper-limit flux for retrieving *ROSAT* data is estimated using the same method as the *ASCA* data, except that the background is taken from a surrounding  $12' \times 12'$  region. *ROSAT* has narrower bandpass (0.1–2.4 keV) than *ASCA*, but it has sharper on-axis *psf*, and therefore is better for source identification especially in a crowded region.

Table 5 and 6 list the detected and non detected sources, respectively. With the *ASCA* satellite, 11 sources are found above the  $5\sigma$  threshold. (V921 Sco is excluded due to difficulty in identification.) The detection rate ( $\sim 31\%$ ) is smaller than that of the *ROSAT* survey ( $\sim 52\%$ , Zinnecker & Preibisch 1994), due mainly to the higher detection threshold to eliminate contamination from nearby bright sources (e.g. AB Aur, HD 97048 and Z CMa). A few embedded sources (e.g. MWC 297 and IRAS 12496-7650) are however detected for the first time in X-rays by *ASCA*, thanks to its hard X-ray imaging capability.

### 3.2. Timing Analysis

We made light curves in the full energy range by subtracting background. The time bin is typically 2048 sec but it is longer for weak sources. The error of each bin is estimated by the Gaussian approximation. Typical net counts per bin of combined SIS and GIS light curves are around 80 counts/bin. We fit the light curves with a constant-flux model using the chi-square method, and find time variable sources with 96% confidence.

Table 7 shows the result of the timing analyses. Four (or five if we include merged light curves of TY CrA and HD 176386 (TYHD)) among twelve detected sources (36–45%) were variable. If we exclude sources with total net counts less than 1000 photons, half (or 3/4 including TYHD) are variable.

### 3.3. Spectra

We fit spectra with an absorbed thin-thermal plasma model (the MeKaL plasma code, Mewe et al. 1995). The response matrixes for the SIS were made with *sisrmg* ver. 1.1, while a standard one was used for the GIS. The ancillary response function for both were made with *ascaarf* ver. 2.81. Chemical abundances are basically fixed at  $0.3Z_{\odot}$ , following the typical value for the stellar X-rays (e.g. OB stars, Kitamoto & Mukai 1996; Kitamoto et al. 2000; low-mass MSs, Tagliaferri et al. 1997; low-mass PMSSs, Yamauchi et al. 1996; Kamata et al. 1997; Tsuboi et al. 1998).

Spectra for most sources except HD 104237 and HD 200775 were fit with either an absorbed one-temperature (1T) or two-temperature (2T) thin-thermal (MeKaL) model (with a Gaussian component for VY Mon) with 90% confidence (Table 8). Unacceptable fits of HD 104237 and HD 200775 seem to be caused by small structures in the spectra, which might be unknown emission lines or absorptions. The best-fit temperature ranges between  $kT \sim 1\text{--}5$  keV, which is significantly higher than the X-ray temperature of MS OB stars ( $kT < 1$  keV, e.g. Corcoran et al. 1994).

## 4. Comments on Individual Sources

This section provides observational details of each detected source: i.e. stellar characteristics and *ASCA* results of imaging, timing and spectral analysis.

### 4.1. V892 Tau

V892 Tau (Elias 3-1) is located in the L1495E dark cloud. The stellar parameters are open to dispute; Strom & Strom (1994) quoted it as a B9 star of  $L_{\text{bol}} \sim 64.3 L_{\odot}$ , while Zinnecker & Preibisch (1994) quoted it as an A6e star of  $L_{\text{bol}} \sim 38 L_{\odot}$ . It has a circumstellar disk of  $\sim 0.1 M_{\odot}$  (di Francesco et al. 1997). There is a companion star (Elias I NE) at  $\sim 4''$  northeast from V892 Tau, which would be a weak line T-Tauri star (WTTS) with  $L_{\text{bol}} \sim 0.3 L_{\odot}$  (Skinner et al. 1993; Leinert et al. 1997; Pirzkal et al. 1997). Strom & Strom (1994) first reported the X-ray emission from V892 Tau ( $\log L_{\text{X}} \sim 30$  ergs s $^{-1}$ ). Zinnecker & Preibisch (1994) measured a plasma temperature of  $\sim 2.3$  keV and hydrogen column density of  $\sim 4.8 \times 10^{21} \text{ cm}^{-2}$ .

V892 Tau is detected as the strongest source in the  $12' \times 12'$  square field (Figure 1a). The SIS image shows two other X-ray sources: V1023 Tau at  $\sim 2'$  northeast from V892 Tau

and V410 X-ray 7 at  $30''$  southeast, which is only obviously seen in the soft band image (0.55–2 keV). V410 X-ray 7 is a reddened M0.5 PMS star (Briceño et al. 1998), from which *ROSAT* detected an X-ray flare (Stelzer et al. 2000). Because the GIS does not resolve V1023 Tau from V892 Tau, we only use the SIS for latter analysis. V892 Tau and V410 X-ray 7 strongly merge together so that V410 X-ray 7 is included in the source region of V892 Tau. The light curve in the total band (Figure 1b) seems to fluctuate by a factor of two, but it accepts a constant model within 90% confidence level, which suggests that neither V892 Tau nor V410 X-ray 7 showed variation. The spectrum can be reproduced by an absorbed 1T thin-thermal model (1T model in Table 8), but it includes a component from V410 X-ray 7. As we see in the SIS hard band image, hard X-ray emission from V410 X-ray 7 is negligible. Because the high energy part of the X-ray emission determines the plasma temperature, we think that the temperature derived in the 1T model represents the temperature of V892 Tau. On the other hand, in the soft band image (0.55–2 keV), V410 X-ray 7 is as bright as V892 Tau, which means that the soft X-ray flux of V892 Tau is half of that of the 1T model. When we only change  $N_{\text{H}}$  parameter of the 1T model to fit the condition,  $N_{\text{H}}$  of V892 Tau is  $\sim 1.8 \times 10^{22} \text{ cm}^{-2}$ . The residual component, which would be attributed to V410 X-ray 7, can be successfully fit by another absorbed 1T model (2T model in Table 8 and Figure 1c).

#### 4.2. V380 Ori

V380 Ori is a B9–A0 star of  $3.3\text{--}3.6 M_{\odot}$  with small amplitude variability (Hillenbrand et al. 1992; Böhm & Catala 1995; Rossi et al. 1999; Herbst & Shevchenko 1999; Rossi et al. 1999). It has a companion star  $0.^{\circ}15$  from the primary (Corporon & Lagrange 1999). X-ray emission was detected with *Einstein* and *ROSAT* ( $\log L_{\text{X}} \sim 31.0\text{--}31.3 \text{ ergs s}^{-1}$ , Pravdo & Marshall 1981; Zinnecker & Preibisch 1994). From the *Einstein* data, the plasma temperature and column density are  $\sim 1.1 \text{ keV}$  and  $7.4 \times 10^{21} \text{ cm}^{-2}$ , respectively (Damiani et al. 1994).

V380 Ori is detected as a relatively faint source (Figure 2a). It is near the edge of the GIS *fov* ( $4'$  inside from the edge) so that the *psf* is less sharp. The light curve shows no apparent variability. The spectral fitting (see Figure 2b) shows relatively high plasma temperature ( $\sim 3.2 \text{ keV}$ ) though the uncertainty (0.7 – 11.0 keV) is large. The luminosity ( $\log L_{\text{X}} \sim 31.2 \text{ ergs s}^{-1}$ ) is about the same as that in the *Einstein* and *ROSAT* observations.

### 4.3. VY Mon & CoKu VY Mon/G2

Both VY Mon and CoKu VY Mon/G2 are members of the Mon OB1 association (Cohen & Kuhi 1979; Testi et al. 1998). VY Mon is a O9–B8 star in very young phase ( $\sim 5 \times 10^4$  years) with Algol-type variability and large IR excess (see Casey & Harper 1990; Thé et al. 1994; Testi et al. 1999). CoKu VY Mon/G2 is a candidate Herbig Ae star (Thé et al. 1994). Damiani et al. (1994) reported X-ray emission from VY Mon and/or CoKu VY Mon/G2 with *Einstein* in the hard band (S/N  $\sim 2.5$ ).

The GIS detects an X-ray source around VY Mon and CoKu VY Mon/G2 at a large off-axis angle ( $\sim 20'$ ), where the absolute position uncertainty is poorly calibrated (a few arc-minutes) (Figure 3a *left*). We thus used a *ROSAT* PSPC image for source identification (Figure 3a *right*). Though all four *ROSAT* observations has relatively large off-axis angle of the source ( $\sim 30'$ ), where 68% of source photons falls within a  $\sim 1'$  radius circle, VY Mon and/or CoKu VY Mon/G2 can be the counterpart of the X-ray source. The *ASCA* light curve (Figure 3b) gradually decreases with small fluctuations and becomes almost constant after  $\sim 6 \times 10^4$  sec. We thus define the phase before  $6 \times 10^4$  sec as the high state (HS) and the phase after as the low state (LS). The low state spectrum has an enhancement at around 5 keV (*left panel* of Figure 3c). An absorbed 1T model with a Gaussian component at  $\sim 5.1$  keV has an acceptable fit in 90% confidence level, but there is no corresponding emission line of abundant elements at the measured energy (e.g. Ca, Fe). We also tried an additional thermal model, but it does not reproduce the strong dip feature at  $\sim 5.3$  keV. The origin of the line emission is unknown. On the other hand, the high state spectrum (*right panel* of Figure 3c) accepts an absorbed 1T model with very high plasma temperature ( $\sim 6$  keV). The X-ray luminosity ( $\log L_X \sim 32.2$  ergs s $^{-1}$ ) is one of the largest among our samples. VY Mon forms a small cluster. The X-ray emission could be from the assembly of cluster members. However, we should note that  $N_{\text{H}}$  does not change between the HS and LS, and corresponds to the  $A_V$  ( $\sim 1.6^m$ ) of CoKu VY Mon/G2.

### 4.4. HD 104237

HD 104237, located in the Chamaeleon III dark cloud, is the brightest HAeBe star in the sky ( $V = 6.6^m$ , Hu et al. 1991). It has the spectral type A4e and would be slightly older than other star HAeBe stars (Age  $\sim 10^{6.3}$  years, Knee & Prusti 1996; van den Ancker et al. 1998). The *ASCA* observation of HD 104237 is described in Skinner & Yamauchi (1996) in detail.

X-ray emission is detected at the position of HD 104237 (Figure 4a). The light curve

(Figure 4b) seems to vary periodically and rejects a constant model. The spectrum (Figure 4c) needs at least 2T components, which still seem to have small deviation. Skinner & Yamauchi (1996) succeeded in reproducing the SIS spectrum by 2T models, but we do not succeed in reproducing both the SIS and GIS spectra simultaneously, though we do not find any systematic difference between the spectra. We also tried to fit the spectra by three models, commonly absorbed 2T model with free elemental abundance, 2T model with different  $N_{\text{H}}$ , and commonly absorbed 3T model, but the reduced  $\chi^2$  value did not improve. The large  $\chi^2$  seems to be caused by weak spectral features (e.g. emission lines). In the discussion section, we refer the physical parameters of HD 104237 to the commonly absorbed 2T model.

#### 4.5. IRAS 12496–7650

IRAS 12496–7650 is an embedded Herbig Ae star (Hughes et al. 1989) and is the most luminous far-infrared source in the Chameleon II cloud. The *ASCA* observation is described in Yamauchi et al. (1998).

The GIS image is shown in Figure 5a. The X-ray spectrum (Figure 5b) shows very large absorption of about  $N_{\text{H}} \sim 10^{23} \text{ cm}^{-2}$ , which is more than five times of the  $N_{\text{H}}$  converted from the  $A_{\text{V}}$  (Hughes et al. 1991). The absorption column is the largest among our sample.

#### 4.6. HR 5999

HR 5999 is a variable A5-7e star with age of  $5 \times 10^5$ -year-old located in the center of the Lupus 3 subgroup (van den Ancker et al. 1998; Tjin A Djie et al. 1989). It is thought to have an accretion disk (e.g. Thé et al. 1996), which might cause photometric and spectral variations. It also has a close companion at 1.3" apart (Rossiter 3930, Stecklum et al. 1995), probably a T-Tauri star (TTS). The X-ray emission of HR 5999 was detected with *ROSAT* (Zinnecker & Preibisch 1994).

HR 5999 is fainter and hidden in the *psf* wings of the intermediate-mass young peculiar star HR 6000. The peak is only recognized in the SIS image (not clear in Figure 6a). To cancel out contamination from HR 6000, we selected a background region symmetric with respect to HR 6000. We do not find any systematic difference in light curve and spectrum between SIS0 and SIS1, which would mean that contamination from HR 6000 is satisfactorily removed. Net event counts within a very small ellipse centered at HR 5999 (see Table 4) is around 50% of total counts of the source region. The SIS spectrum of HR 5999 is reproduced by

an absorbed 1T thermal model (Figure 6b). The  $N_{\text{H}}$  error range ( $<1.2 \times 10^{22} \text{ cm}^{-2}$ ) includes the  $N_{\text{H}}$  converted from  $A_{\text{V}}$  ( $\sim 0.5^m$ ). The temperature is consistent with the hot component seen in the *ROSAT* spectrum (1T model in Table 8), and become closer to it by assuming the same  $N_{\text{H}}$  as in the *ROSAT* analysis (1T<sup>F</sup> model in Table 8, Zinnecker & Preibisch 1994). The consistency between  $N_{\text{H}}$  and  $A_{\text{V}}$  and larger  $L_{\text{X}}$  than in low-mass stars (see discussion 5.1) suggests that the detected X-ray emission is from HR 5999.

#### 4.7. V921 Sco

V921 Sco (CoD  $-42^{\circ} 11721$ ) is located in the galactic plane  $[(l, b) = (343.35, -0.08)]$ . Some papers classify it as a supergiant (e.g. Hutsemékers & van Drom 1990). The distance to V921 Sco has large uncertainty from 200 pc to 2.6 kpc (Pezzuto et al. 1997; Brooke et al. 1993). We adopt the distance of 500 pc derived from a spectral analysis with the ISO–SWS (Benedettini et al. 1998).

A weak X-ray source is detected on the GIS image (Figure 7a). The source is seen as two marginal humps in the SIS, which might mean that the X-ray emission is from multiple nearby sources. Actually V921 Sco, which is in the crowded region on the galactic plane, have  $\sim 50$  2MASS sources within  $1'$  though some of them could be nebulae. We thus show the result of timing and spectral analysis, but do not include the source for studies in the discussion sections. The GIS spectrum (Figure 7b) can be reproduced by an absorbed 1T model with strong absorption ( $N_{\text{H}} \sim 5 \times 10^{22} \text{ cm}^{-2}$ ). The  $N_{\text{H}}$  is significantly higher than  $N_{\text{H}}$  converted from its  $A_{\text{V}}$  ( $N_{\text{H}} \sim 1.6 \times 10^{22} \text{ cm}^{-2}$ ), though it is consistent with  $N_{\text{H}}$  derived from a millimeter survey ( $\sim 10^{23} \text{ cm}^{-2}$ , Henning et al. 1998).

#### 4.8. MWC 297

MWC 297 is a highly reddened star with extremely strong Balmer and silicate lines. Hillenbrand et al. (1992) reported that MWC 297 is a PMS star with the spectral type of O9 at a distance of 450 pc and age of  $\sim 3 \times 10^4$  years. Drew et al. (1997), however, suggested it to be a B1.5 zero-age main-sequence (ZAMS) star at the distance of  $\sim 250$  pc. They also argued that MWC 297 is a rapid rotator with  $v_{\text{rot}} \sin i \sim 350 \text{ km s}^{-1}$ . The *ASCA* observation of MWC 297 is described in Hamaguchi et al. (2000). Here, the X-ray luminosity is smaller than that in Hamaguchi et al. (2000) because we assume a distance of 250 pc.

A point-like X-ray source is detected in three observations spanning 5 days. Figure 8a shows the SIS image from the 1st observation (MWC297 1). We also checked a *ROSAT*

observation of the MWC 297 field (exposure  $\sim 1$  ksec), but we found no X-ray source in the field. The combined light curves of the three observations (Figure 8b) show that the X-ray flux in the first observation is constant, but increased by a factor of five at the beginning of the second observation, then gradually decreased exponentially to nearly the same flux of the pre-flare level by the end of the third observation with an  $e$ -folding time  $\sim 5.6 \times 10^4$  sec. SIS spectra of all observations are separately displayed in Figure 8c. The absorption column  $\sim 2.4 \times 10^{22}$  cm $^{-2}$  did not change during the observations. The plasma temperature in the quiescent phase of 3.4 keV increased to 6.5 keV during the flare and then decreased to 3.4 keV. The flare peak was missed; we only detected X-rays after the on-set of the flare. Thus, the peak luminosity is  $\log L_X \gtrsim 32.1$  ergs s $^{-1}$ , which is the maximum at the beginning of the second observation. A giant X-ray flare from the early MS star  $\lambda$  Eridani (B2e) was detected by *ROSAT* (Smith et al. 1993). The star would be young and would not be a classical Be star. The flare detected on MWC297 might have some relation in mechanism to  $\lambda$  Eridani.

#### 4.9. TY CrA / HD 176386

TY CrA and HD 176386 belong to the R CrA cloud and illuminate the reflection nebula NGC 6726/7 (Graham 1991). TY CrA is a detached Herbig Be eclipsing binary consistency of a  $3.16M_\odot$  primary star near ZAMS and a  $1.64M_\odot$  secondary star with an orbital period of  $\sim 2.889$  days (Kardopolov et al. 1981; Casey et al. 1993, 1995, 1998). Both stars are  $\sim 3 \times 10^6$ -year-old. The lack of infrared excess indicates absence of an optically thick disk (Casey et al. 1993). It shows non-thermal radio emission (Skinner et al. 1993). The X-ray emission is detected by *Einstein* and *ROSAT*. Damiani et al. (1994) measured the plasma temperature at  $\sim 1$  keV and the absorption column density at  $\sim 5.5 \times 10^{21}$  cm $^{-2}$ . On the other hand, HD 176386 is a B9.5 star close to the ZAMS with mid-infrared excess but no H $\alpha$  emission reported ( $2.8 \times 10^6$ -year-old, Bibo et al. 1992; Grady et al. 1993; Prusti et al. 1994; Siebenmorgen et al. 2000).

Both TY CrA and HD 176386 exhibit X-ray emission (Figure 9a). We focus on the SIS data taken in 3 observations (R CrA 1, 4 and 6) because the GIS cannot resolve TY CrA and HD 176386, but the SIS marginally does. We selected a background at the symmetrical region with respect to each source to cancel contamination from each other. All light curves are constant in each observation, and the average flux does not change between observations. Spectra of both TY CrA and HD 176386 can be fit by an absorbed 1T model (Figure 9c). For the three observations, the best-fit column density and plasma temperature for TY CrA are  $3-6 \times 10^{21}$  cm $^{-2}$  and 1–2 keV respectively, which are the same as the *Einstein* result (Damiani et al. 1994). The fits to the HD 176386 spectrum have two local  $\chi^2$  minima, among

which smaller  $N_{\text{H}}$  ( $<2 \times 10^{21} \text{ cm}^{-2}$ ) is consistent with the  $A_{\text{V}}$ <sup>1</sup>. The plasma temperature is around 1–2 keV. On the other hand, at the end of R CrA 3 in which only GIS data is available and hence X-ray emission from TY CrA and HD 176386 is merged together, we see a flare like variation with long rise time ( $\sim 10$  ksec, see also Table 9) as a stellar flare (Figure 9b). We define the high flux state HS and the other LS, and tentatively fit the spectra by an absorbed 1T model. Then the best-fit plasma temperature is slightly higher during HS ( $kT \sim 3.0$  keV) with respect to LS ( $kT \sim 2.6$  keV). Because the rise time-scale is too long for a normal stellar flare, the flare might relate to binary interaction. The peak came after 80 ksec of the eclipse of the primary star, equivalent to  $\sim 120^\circ$  rotation of the binary system, when we see  $\sim 2/3$  of the surface of the companion facing the primary star. The flare may occur on an active spot of the companion at the root of inter-binary magnetic field.

#### 4.10. HD 200775

HD 200775 is a B2.5e star illuminating the reflection nebula NGC 7023 (van den Ancker et al. 1998; Benedettini et al. 1998). It is in a biconical cavity that has been swept away by energetic bipolar outflows, but there is no evidence of ongoing outflow activity (Fuente et al. 1998). Its age is estimated to be  $\sim 2 \times 10^4$  years from the HR diagram, but it might be  $2 \times 10^7$  year-old in the post main-sequence stage (van den Ancker et al. 1997). HD 200775 has a companion star  $2.^{\circ}25$  apart ( $\Delta K = 4.9^m$ , Li et al. 1994; Pirzkal et al. 1997). Damiani et al. (1994) detected strong X-ray emission with *Einstein* ( $\log L_{\text{X}} \sim 31.9 \text{ ergs s}^{-1}$ ) and measured  $N_{\text{H}} \sim 5 \times 10^{21} \text{ cm}^{-2}$  and  $kT \sim 0.8$  keV.

A point-like source was detected at the position of HD 200775 (Figure 10a). The SIS0 light curve has a spike at about  $9.3 \times 10^4$  sec, which is probably an instrumental artifact. The other light curves (SIS1, GIS) show marginal flux increases around 2, 4 and  $10 \times 10^4$  sec, and the light curve rejects a constant model above 96% confidence level. (Figure 10b). The spiky event does not have significant counts so that we use all the SIS and GIS data for spectral fitting (Figure 10c). An absorbed 1T model is rejected over 99.9% confidence. An absorbed 2T model with common  $N_{\text{H}}$  improves the reduced  $\chi^2$  value to 1.15 and is accepted above 90% confidence. However, the  $N_{\text{H}}$  value ( $\sim 9 \times 10^{21} \text{ cm}^{-2}$ ) is two times as large as the converted  $N_{\text{H}}$  from visual extinction of HD 200775 ( $A_{\text{V}} \sim 1.9^m$ ). Marginal bumpy features are present in the 2–4 keV band. We thus tried these two models: (i) 2T thermal model

---

<sup>1</sup>Cardelli & Wallerstein (1989) suggested  $R_{\text{V}}$  to the direction of TY CrA considerably high compared with normal regions, and derived larger  $A_{\text{V}}$  ( $\sim 3.1^m$ ) than Hillenbrand et al. (1992) ( $A_{\text{V}} \sim 1.0^m$ ). However, the  $A_{\text{V}} - N_{\text{H}}$  relation in Ryter (1996) assumes  $R_{\text{V}}$  at 3.1. We therefore refer to Hillenbrand et al. (1992).

with a free abundances, (ii) 1T thermal and hard power-law model. In the model (i), the metal abundance is slightly larger (0.39 solar) than the fixed abundance (0.3 solar), but the model fit does not improve. On the other hand, the best-fit  $N_{\text{H}}$  of the model (ii) is  $\sim 4 \times 10^{21} \text{ cm}^{-2}$ , which is almost equal to the  $N_{\text{H}}$  converted from  $A_{\text{V}}$  though we do not have physical interpretation to explain the power-law component.

#### 4.11. MWC 1080

MWC 1080 is an early A type star with  $A_{\text{V}} \sim 4.4^m$  (Yoshida et al. 1992). The distance is 2.2–2.5 kpc from UVBR photometry of neighboring MS stars (Grankin et al. 1992) and kinematic distance of  $^{13}\text{CO}$  molecular line (Cantó et al. 1984). It forms a multiple system of a HAeBe primary, a plausible HAeBe companion (0.7") and another companion (4.7"), with eclipse events at  $\sim 2.887$  days (Grankin et al. 1992; Leinert et al. 1997; Pirzkal et al. 1997). It has CO molecular outflow and ionizing winds up to  $1000 \text{ km s}^{-1}$  (Cantó et al. 1984; Yoshida et al. 1992; Leinert et al. 1997; Benedettini et al. 1998). The X-ray emission was detected with *ROSAT* (Zinnecker & Preibisch 1994,  $\log L_{\text{X}} \sim 32 \text{ ergs s}^{-1}$ ).

An X-ray source was detected near MWC 1080 (Figure 11a). The light curves (Figure 11b) seem to oscillate periodically by  $\sim 40$  ksec, but this is not statistically significant. The orbital phase during the observation is  $\phi = 0.39$  to 0.74 according to the ephemeris by Grankin et al. (1992). The secondary eclipse occurs at  $3 \times 10^4$  sec, but it is not observed in the X-ray light curve. The light curves do not show evidence that binarity affects the observed X-ray emission of MWC 1080. The spectrum (Figure 11c) can be reproduced by an absorbed 1T model. The temperature is extremely high ( $kT > 3.8 \text{ keV}$ ) and the absorption column density ( $N_{\text{H}} \sim 10^{22} \text{ cm}^{-2}$ ) is consistent with  $A_{\text{V}}$ . The spectrum has an excess around 6–7 keV. When we include a Gaussian model with  $\sigma = 0.0$ , the center energy is 6.4 (6.2–6.6) keV, which corresponds to the iron fluorescent line. On the other hand, an absorbed 1T model with the free abundance parameter has abundance of 0.8 solar, which is mainly determined from Helium-like Fe-K line emission. The residual still seems to have systematic patterns though the model is accepted  $> 90\%$  confidence. A commonly absorbed 2T model or soft 1T + power-law model compensate the pattern slightly better, but the best-fit  $N_{\text{H}}$  ( $\sim 5 \times 10^{22} \text{ cm}^{-2}$ ) is large and luminosity of the best-fit model is unrealistically high for stellar X-ray emission ( $> 10^{36} \text{ ergs s}^{-1}$ ).

#### 4.12. EC 95

Preibisch (1998) first reported constant X-ray emission from EC 95. From near-infrared spectroscopy, Preibisch (1999) determined EC 95 as an extremely young intermediate-mass star (Age  $\sim 2 \times 10^5$  years;  $M \sim 4 M_\odot$ ), a so called proto-HAeBe. The very high visual extinction ( $A_V \sim 25-35^m$ ) made them suspect that the source has a large intrinsic X-ray luminosity of about  $\log L_X \sim 33$  ergs s $^{-1}$ . Radio observations have detected a point-like source, SH 68-2, within the error circle of EC 95 (Rodriguez et al. 1980; Snell & Bally 1986; Smith et al. 1999), showing gyrosynchrotron emission suggesting presence of a magnetosphere.

A point-like source is detected within the error circle of EC 95 (Figure 12a). The nearest *ROSAT* X-ray source is 1. $'$ 5 apart (Preibisch 1998). *ASCA* would see the same source. The light curves show flare-like small fluctuations and reject a constant model (Figure 12b). Spectra of the SIS and GIS (Figure 12c for the SIS) are inconsistent in absolute flux. The SIS flux calibration is less reliable due to CCD degradation. We independently varied the model normalizations, and find an acceptable result. The flux is derived from the GIS data. The plasma temperature is quite high ( $kT \sim 3.9$  keV).  $N_H$  is large but about one fourth of the  $A_V$  ( $\sim 36^m$ ) converted  $N_H$ . The luminosity ( $\log L_X \sim 31.7$  ergs s $^{-1}$ ) is therefore about an order of mag smaller than the *ROSAT* estimate.

### 5. X-ray Emission Mechanism

#### 5.1. Could the X-ray Emission Come from a Low-Mass Companion?

More than 85% of HAeBes are visible or spectroscopic binaries (Pirzkal et al. 1997), whose companions could be low-mass stars, i.e. TTSs or protostars. Low-mass stars are known to emit strong X-rays compared with their faint optical and IR emission ( $L_X/L_{bol}$  up to  $10^{-3}$ ). We thus evaluate as whether the X-ray emission observed with *ASCA* could come from low-mass stars. Stelzer & Neuhäuser (2001) reports that, in the Taurus Auriga region, CTTSs and WTTSs with  $\log L_X \gtrsim 30$  ergs s $^{-1}$  are around 5% and 25%, respectively. Multiplying the binary ratio, around 4% and 20% of the X-ray emission with  $\log L_X \gtrsim 30$  ergs s $^{-1}$  could be really from low-mass companions. *ASCA* detected sources have  $\log L_X \gtrsim 30$  ergs s $^{-1}$  and the detection rate is  $\sim 30\%$ . Contribution of the companion could be non-negligible if the companions follow the luminosity function of WTTSs. However, considering that the primary star and its companion tend to have similar ages (e.g. see Casey et al. (1998) for TY CrA), CTTSs with the similar ages to HAeBes ( $\sim 10^6$ -year-old) might be more appropriate for this estimate, then the contribution of the companion in our sample would be negligible. While there are almost no TTSs above  $10^{31}$  ergs s $^{-1}$ , therefore the X-ray

emission would be responsible for the primary (i.e. early-type) star.

## 5.2. X-ray Properties

The X-ray properties of HAeBes and their relation to the stellar parameters may provide further insight into the origin of the X-ray emission. In this section, we examine the relation of  $L_X$  to other stellar parameters such as  $L_{\text{bol}}$ ,  $T_{\text{eff}}$  and  $v_{\text{rot}} \sin i$ , the X-ray time variability and the plasma temperature. We then compare the properties with those of low-mass and high-mass stars. In the discussion of X-ray luminosity, we included *ROSAT* samples of HAeBes (Zinnecker & Preibisch 1994). Their  $L_X$  in the *ASCA* band (0.5–10 keV) is estimated by assuming an absorbed thin-thermal model with  $kT = 2$  keV, abundance =  $0.3Z_{\odot}$  and  $N_{\text{H}}$  converted from  $A_{\text{V}}$  (Ryter 1996). The errors are put between half and factor of two of their  $L_X$  to allow for uncertainty of  $kT \sim 0.5$ –4 keV. The photon statistical errors are basically much smaller than this error range. Whereas, we also include EC 95 and SSV 63E+W as candidates of proto-HAeBes. SSV 63E+W is either a Class I protostar candidate SSV 63E or W in the Orion cloud. Zealey et al. (1992) mention that SSV 63E may have mass  $1.5M_{\odot} < M < 5M_{\odot}$  assuming age less than  $10^6$ -years at a distance of 460 pc. The X-ray emission is reported by Ozawa et al. (1999). On the other hand, we did not include V921 Sco in the sample.

Figure 13a shows the  $L_X$  vs.  $L_{\text{bol}}$  diagram. In our HAeBe samples ranging between  $33 < \log L_{\text{bol}} \text{ ergs s}^{-1} < 38$ , the  $\log L_X/L_{\text{bol}}$  ratio is between  $-4$  and  $-7$ . The ratio is above the range of massive MS stars ( $-6 \sim -8$ ), and rather close to, but slightly different from, that of low-mass stars (up to  $-3$ ) (e.g. Gagné et al. 1995). The  $L_X/L_{\text{bol}}$  ratio of proto-HAeBe is close to  $-3$ . This might suggest that X-ray activity is enhanced in the very youngest stars (see also discussion in the section 5.3). Figure 13b shows the dependence of  $\log L_X/L_{\text{bol}}$  on  $\log T_{\text{eff}}$ . The  $\log L_X/L_{\text{bol}}$  increases as  $\log T_{\text{eff}}$  decreases, which resembles the trend of X-ray sources in the Orion cloud (Fig. 8 in Gagné et al. 1995). Figure 13c shows the  $\log L_X/L_{\text{bol}}$  dependence on  $v_{\text{rot}} \sin i$  (Grady et al. 1993; Böhm & Catala 1995; Drew et al. 1997; Casey et al. 1998; van den Ancker et al. 1998; Corporon & Lagrange 1999). The  $\log L_X/L_{\text{bol}}$  of low-mass MS stars saturates at  $\sim -3$  above  $v_{\text{rot}} \sin i > 15 \text{ km s}^{-1}$  (Stauffer et al. 1994), which represents a saturated dynamo on solar-like low-mass stars. Log  $L_X/L_{\text{bol}}$  for HAeBes is rather small for high  $v_{\text{rot}} \sin i$ , and does not seem to saturate at any specific velocity. The activity might not be generated by a magnetic dynamo as in solar-like low-mass stars.

The plasma temperature of HAeBes ( $kT \sim 2$  keV) is significantly higher than the typical temperature of high-mass MS stars, which is driven by high speed stellar winds ( $kT \sim 1$  keV,  $v_{\text{wind}} \sim 1000$ –3000  $\text{km s}^{-1}$ ). We calculate the maximum plasma temperature produced

by HAeBe stellar winds (Nisini et al. 1995; Benedettini et al. 1998) assuming that all wind kinetic energy is thermalized (Figure 14). Then the plasma temperature observed with *ASCA* is above the maximum temperature which can be made by HAeBe winds. While, X-ray emission from  $\sim 2$  keV plasma is usually seen on TTSs and protostars with magnetic activity.

MWC 297, VY Mon and TY CrA exhibited prominent variability (see Table 9). MWC 297 and TY CrA had strong flux increase from the pre-flare level and exponential decay seen on low-mass stellar flares, while VY Mon had rather steady decay. Variations of MWC 297 and TY CrA strongly indicate a flare magnetic activity although they could be on their companions. Their decay timescales derived by exponential model fits (10–60 ksec) are longer than those of low-mass MS and TTS flares (2–7 ksec, Stelzer et al. 2000) and as long as the flare decay of protostars (10–30 ksec, Tsuboi et al. 2000). X-ray flares on HAeBes might be similar to those on protostars.

Plasma temperatures and variability are similar to those of low-mass stars. This may suggest that X-ray emission from HAeBes originates from magnetic activity. We have enough reason to believe it because optical observations suggest that some HAes have azimuthal magnetic fields (AB Aur: MgII 2795Å, Praderie et al. 1986; HeI 5876Å, Böhm et al. 1996). On the other hand, the  $L_X/L_{\text{bol}}$  ratio and its dependence on stellar rotational velocity is different from those of low-mass stars, which may mean that magnetic activity is not by a magnetic dynamo. Actually, the stellar evolutional model of intermediate-mass stars (Palla & Stahler 1990) predicts the absence of a surface convection zone necessary for a solar type dynamo. Another type of magnetic activity might be required for HAeBes.

### 5.3. Evolution of Stellar X-ray Activity

Circumstellar gases gradually dissipate through mass accretion, outflows and stellar winds. The hydrogen column density along the line of sight therefore decreases with age, although it might also depends on stellar mass, disk inclination and so on. We thus regard  $N_{\text{H}}$  as a rough indicator of stellar age. We then see  $kT$  rises from 2 to 5 keV as  $N_{\text{H}}$  increases (Figure 15). Points in the high  $N_{\text{H}}$  low  $kT$  area are missing simply because of the weak sensitivity to soft X-ray emission from large  $N_{\text{H}}$  sources, but plasma temperature tends to increase with  $N_{\text{H}}$ . Younger HAeBes tend to have hotter temperature.

$L_X$  does not have clear correlation with  $N_{\text{H}}$ . We thus make a bubble chart of  $L_X$  in the HR diagram (Figure 16). Sources in the upper right region in the diagram have  $\log L_X \sim 32$  ergs  $\text{s}^{-1}$  and gradually decrease as they come close to the MS branch. A notable feature is

the presence of an *X-ray inactive region* in the HR diagram:  $3.8 < \log T_{\text{eff}} (\text{K}) < 4.1$  and  $1.3 < \log L_{\text{bol}} (L_{\odot}) < 1.9$ , which corresponds to the age older than  $10^6$ -year-old. Almost no source in this region has  $\log L_{\text{X}} (\text{ergs s}^{-1}) > 30$ . This *X-ray inactive region* may indicate that X-ray activity of HAeBes terminates after the age of  $\sim 10^6$ -year-old. Damiani et al. (1994) found a correlation between  $L_{\text{X}}$  and spectral type or  $L_{\text{bol}}$ , but Zinnecker & Preibisch (1994) did not. We now see that this difference is simply due to selection effects. Damiani et al. (1994) collected HAeBe samples close to the MS so that they found a similar X-ray characteristics to MS stars. Zinnecker & Preibisch (1994) examined young A-type samples such as V380 Ori and HR 5999. Their X-ray luminosity is comparable to early B-type stars and thus has no dependence on stellar spectral type.

The above discussion suggests that the X-ray activity decays with age and falls below  $\log L_{\text{X}} (\text{ergs s}^{-1}) \sim 30$  at  $\sim 10^6$ -years-old. This age coincides with the end phase of outflow activity (Fuente et al. 1998). We therefore hypothesize that X-ray activity of HAeBes is triggered by reconnection of magnetic fields linking a star and its circumstellar disk (a star and disk dynamo activity) as it was claimed for the X-ray emission mechanism of low-mass protostars (e.g. Koyama et al. 1996; Hayashi et al. 1996; Montmerle et al. 2000). This model reconciles the lack of a magnetic dynamo on the stellar surface of HAeBes. To test the hypothesis, we correlate  $L_{\text{X}}$  of HAeBes with outflow activity by referring to tables in Maheswar et al. (2002) and Lorenzetti et al. (1999) and several individual papers (Table 10). Then, sources with  $\log L_{\text{X}} > 30 \text{ ergs s}^{-1}$  tend to have outflow activity, which might suggest a link between X-ray and outflow activity. Identification of outflow sources especially in crowded regions (e.g. EC 95, R CrA, T CrA) seems to have uncertainty, while the outflow from HD 200775 could be made by stellar winds (Fuente et al. 1998). More careful study would be required.

Our results suggest that X-ray emission from young HAeBes originates in magnetic activity. This means that magnetic activity plays an important role for both low-mass and intermediate-mass PMSs. We here propose a unified scenario for the X-ray activity of PMSs. In this scenario, stellar X-ray emission begins in the protostar phase when stars are deeply embedded in molecular cloud cores. In this phase, stars possess fossil magnetic fields from their parent clouds and exhibit violent magnetic activity linking a star and its disk, showing occasional X-ray flares. A part of the infalling gases goes out from the system with large amounts of angular momentum, which is later seen as molecular outflows or optical jets. After the star-disk dynamo activity disappears in  $\sim 10^6$ -year-old, low-mass stars still continue magnetic activity similar to a solar type dynamo. Stars between A - F5 lack any mechanism to produce hot plasma. X-ray activity ends for these stars, and the *X-ray inactive region* is seen in the HR diagram.

## 6. Relation of X-ray Activity to MS OB Stars

Figure 16 does not show any clear decrease of X-ray activity on B-type stars ( $\log T_{\text{eff}} \gtrsim 4$  (K)), but the  $L_{\text{X}}-L_{\text{bol}}$  ratio of Herbig Be stars is larger than MS B-type stars (see Figure 13b), which suggests some transition of X-ray activity close to the MS stage. We superimpose our HAeBe data on the  $L_{\text{X}}-L_{\text{bol}}$  graph of OB stars in the sky using *ROSAT* all-sky survey data (Figure 17a, the relation of OB stars referred to Berghöfer et al. 1997). Then, most of the HAeBe samples are above the higher end of OB MS stars. This would mean some transition of X-ray activity between HAeBe and MS phases. B-type stars are not generally thought to have accretion disks. The result may strengthen the star-disk dynamo hypothesis. On the other hand, we do not see any clear gap between MS and HAeBe plots. Berghöfer et al. (1997) suggests that the  $L_{\text{X}}/L_{\text{bol}}$  relation of early-type stars ( $\log L_{\text{X}}/L_{\text{bol}} \sim -7$ ), which is characteristic of a stellar wind origin, scatters later than B1–1.5 stars. This might imply that X-ray activity of HAeBes holds in the early stage of MS B-type stars.

Though no relation to the stellar evolution is claimed between O stars and HAeBes, comparison of their X-ray properties may help to understand X-ray activity. We thus made a  $kT$  and  $L_{\text{X}}$  graph (Figure 17b) of both types of stars (O stars—  $\delta$  Ori,  $\lambda$  Ori; Corcoran et al. 1994;  $\tau$  Sco; Cohen et al. 1997;  $\zeta$  Oph,  $\zeta$  Ori; Kitamoto et al. 2000).  $L_{\text{X}}$  for O stars are calculated from *E.M.* and  $kT$  from their references, using XSPEC 9.0. Some O stars have hard X-ray tail (e.g. Corcoran et al. 1993; Kitamoto & Mukai 1996), which is separately shown in the figure. The hard tail component seems to share the region with HAeBe X-rays, while soft X-rays from O stars do not. Our results may suggest that the hard X-ray tail and HAeBe X-ray activity have something in common (e.g. high energy activity of fossil magnetic fields) though samples are quite limited.

## 7. Conclusion

X-ray emission from HAeBes has long been a puzzle. This is partly because the proper X-ray emission mechanism is not known for these intermediate-mass young stars and partly because satisfying observing results have not been obtained. By combining our *ASCA* analyses with previous *ROSAT* result, we find that the X-ray emission from HAeBes may originate in magnetic activity, which begins in the earliest phase of stars and continues to the MS stage. We list the results and implications below.

1. In the analyses of the *ASCA* data, 11 X-ray counterparts are detected. The X-ray luminosity ranges between  $\log L_{\text{X}} = 30 - 32$  ergs  $\text{s}^{-1}$ , which is significantly larger than the typical luminosity of low-mass stars.

2. Four (or five if we include TYHD) sources of the 11 detected sources (36–45%) exhibited time variation. Three HAeBes showed prominent variations with longer decay time scale (10–60 ksec).
3. X-ray spectra are reproduced by absorbed one or two temperature thin-thermal (MeKaL) models. The plasma temperature ranges between  $kT \sim 1\text{--}5$  keV, which is significantly higher than those of MS OB stars ( $kT < 1$  keV).
4. HAeBes have similar characteristics to low-mass YSOs in plasma temperature and time variability, but not in the  $L_X/L_{\text{bol}}$  ratio and  $v_{\text{rot}} \sin i$  dependence. X-ray emission might originate from magnetic activity, but the activity might not be produced by solar-type magnetic dynamo.
5. If  $N_{\text{H}}$  is an indicator of stellar age, younger HAeBes tend to have hotter plasma. While  $L_X$  goes down below  $10^{30}$  ergs s $^{-1}$  after the stellar age of  $\sim 10^6$ -year-old. We propose that X-ray activity of HAeBes might be driven by magnetic interaction of a fossil field between the star and its accretion disk.

For statistical analyses of young intermediate and high-mass stars, *Chandra* will provide sophisticated data with little source contamination. Time profiles with high photon statistics can be obtained by *XMM-Newton*. While the micro-calorimeter onboard Astro-E2 will provide a powerful tool for performing high resolution spectroscopy in the hard X-rays above 2 keV.

We greatly appreciate useful comments to Thierry Montmerle, Beate Stelzer, Nicholas E. White and Michael F. Corcoran. We also thank the referee for valuable comments that have led to substantial improvements in the analysis and presentation of the paper. This work is performed while the author (K.H.) held awards by the Japan Society for the Promotion of Science for Young Scientists (JSPS), National Space Development Agency of Japan (NASDA) and National Research Council Research Associateship Award at NASA/GSFC. The data in the article is obtained from the High Energy Astrophysics Division Online Service, provided by Institute of Space and Astronautical Science (ISAS) and the High Energy Astrophysics Science Archive Research Center Online Service, provided by the NASA/Goddard Space Flight Center.

## REFERENCES

Benedettini, M., Nisini, B., Giannini, T., Lorenzetti, D., Tommasi, E., Saraceno, P., & Smith, H. A. 1998, *A&A*, 339, 159

Berghöfer, T. W., Schmitt, J. H. M. M., Danner, R., & Cassinelli, J. P. 1997, *A&A*, 322, 167

Bertout, C., Robichon, N., & Arenou, F. 1999, *A&A*, 352, 574

Bibo, E. A., Thé, P. S., & Dawanas, D. N. 1992, *A&A*, 260, 293

Böhm, T., & Catala, C. 1995, *A&A*, 301, 155

Böhm, T., Catala, C., Donati, J. F., Welty, A., Baudrand, J., Butler, C. J., Carter, B., Collier-Cameron, A., Czarny, J., Foing, B., Ghosh, K., Hao, J., Houdebine, E., Huang, L., Jiang, S., Neff, J. E., Rees, D., Semel, M., Simon, T., Talavera, A., Zhai, D., & Zhao, F. 1996, *A&AS*, 120, 431

Briceño, C., Hartmann, L., Stauffer, J., & Martín, E. 1998, *AJ*, 115, 2074

Brooke, T. Y., Tokunaga, A. T., & Strom, S. E. 1993, *AJ*, 106, 656

Burke, B. E., Mountain, R. W., Daniels, P. J., & Dolat, V. S. 1994, *IEEE Trans. NS-41*, 375

Cantó, J., Rodríguez, L. F., Calvet, N., & Levreault, R. M. 1984, *ApJ*, 282, 631

Cardelli, J. A., & Wallerstein, G. 1989, *AJ*, 97, 1099

Casanova, S., Montmerle, T., Feigelson, E. D., & André, P. 1995, *ApJ*, 439, 752

Casey, B. W., Mathieu, R. D., Suntzeff, N. B., Lee, C., & Cardelli, J. A. 1993, *AJ*, 105, 2276

Casey, B. W., Mathieu, R. D., Suntzeff, N. B., & Walter, F. M. 1995, *AJ*, 109, 2156

Casey, B. W., Mathieu, R. D., Vaz, L. P. R., Andersen, J., & Suntzeff, N. B. 1998, *AJ*, 115, 1617

Casey, S. C., & Harper, D. A. 1990, *ApJ*, 362, 663

Cohen, D. H., Cassinelli, J. P., & Waldron, W. L. 1997, *ApJ*, 488, 397

Cohen, M., & Kuhi, L. V. 1979, *ApJS*, 41, 743

Corcoran, D., & Ray, T. P. 1995, *A&A*, 301, 729

Corcoran, M. F., Swank, J. H., Serlemitsos, P. J., Boldt, E., Petre, R., Marshall, F. E., Jahoda, K., Mushotzky, R., Szymkowiak, A., Arnaud, K., Smale, A. P., Weaver, K., & Holt, S. S. 1993, *ApJ*, 412, 792

Corcoran, M. F., Waldron, W. L., MacFarlane, J. J., Chen, W., Pollock, A. M. T., Torii, K., Kitamoto, S., Miura, N., Egoshi, M., & Ohno, Y. 1994, *ApJ*, 436, L95

Corporon, P., & Lagrange, A. M. 1999, *A&AS*, 136, 429

Damiani, F., Micela, G., Sciortino, S., & Harnden, F. R. J. 1994, *ApJ*, 436, 807

di Francesco, J., Evans, N. J., Harvey, P. M., Mundy, L. G., Guilloteau, S., & Chandler, C. J. 1997, *ApJ*, 482, 433

Dotani, T., Yamashita, A., Ezuka, H., Takahashi, K., Crew, G., Mukai, K., & the SIS team. 1997, "Recent Progress of SIS Calibration and Software", Tech. Rep. 5, ISAS

Drew, J. E., Busfield, G., Hoare, M. G., Murdoch, K. A., Nixon, C. A., & Oudmaijer, R. D. 1997, *MNRAS*, 286, 538

Eiroa, C., & Casali, M. M. 1989, *A&A*, 223, L17

Feigelson, E. D., Casanova, S., Montmerle, T., & Guibert, J. 1993, *ApJ*, 416, 623

Fuente, A., Martín-Pintado, J., Rodríguez-Franco, A., & Moriarty-Schieven, G. D. 1998, *A&A*, 339, 575

Gagné, M., Caillault, J. P., & Stauffer, J. R. 1995, *ApJ*, 445, 280

Gotthelf, E. V., Ueda, Y., Fujimoto, R., Kii, T., & Yamaoka, K. 2000, *ApJ*, 543, 417

Grady, C. A., Pérez, M. R., & Thé, P. S. 1993, *A&A*, 274, 847

Graham, J. A. 1991, "Star Formation in the Corona Australis Region", Tech. Rep. 11, ESO

Grankin, K. N., Shevchenko, V. S., Chernyshev, A. V., Ibragimov, M. A., Kondratiev, W. B., Melnikov, S. Y., Yakubov, S. D., Melikian, N. D., & Abramian, G. V. 1992, *Informational Bulletin on Variable Stars*, 3747, 1

Hamaguchi, K., Terada, H., Bamba, A., & Koyama, K. 2000, *ApJ*, 532, 1111

Hayashi, M. R., Shibata, K., & Matsumoto, R. 1996, *ApJ*, 468, L37

Henning, T., Burkert, A., Launhardt, R., Leinert, C., & Stecklum, B. 1998, *A&A*, 336, 565

Herbig, G. H. 1960, *ApJS*, 4, 337

Herbst, W., & Shevchenko, V. S. 1999, *AJ*, 118, 1043

Hillenbrand, L. A., Strom, S. E., Vrba, F. J., & Keene, J. 1992, *ApJ*, 397, 613

Hu, J. Y., Blondel, P. F. C., Catala, C., Talavera, A., Thé, P. S., Tjin A Djie, H. R. E., & de Winter, D. 1991, *A&A*, 248, 150

Hughes, J. D., Emerson, J. P., Zinnecker, H., & Whitelock, P. A. 1989, *MNRAS*, 236, 117

Hughes, J. D., Hartigan, P., Graham, J. A., Emerson, J. P., & Marang, F. 1991, *AJ*, 101, 1013

Hutsemékers, D., & van Drom, E. 1990, *A&A*, 238, 134

Kamata, Y., Koyama, K., Tsuboi, Y., & Yamauchi, S. 1997, *PASJ*, 49, 461

Kardopolov, V. I., Sahanionok, V. V., & Philipjev, G. K. 1981, *Peremennye Zvezdy*, 21, 589

Kitamoto, S., & Mukai, K. 1996, *PASJ*, 48, 813

Kitamoto, S., Tanaka, S., Suzuki, T., Torii, K., Corcoran, M. F., & Waldron, W. 2000, *Advances in Space Research*, 25, 527

Knee, L. B. G., & Prusti, T. 1996, *A&A*, 312, 455

Koyama, K., Hamaguchi, K., Ueno, S., Kobayashi, N., & Feigelson, E. D. 1996, *PASJ*, 48, L87

Leinert, C., Richichi, A., & Haas, M. 1997, *A&A*, 318, 472

Li, W., Evans, N. J., Harvey, P. M., & Colomé, C. 1994, *ApJ*, 433, 199

Lorenzetti, D., Tommasi, E., Giannini, T., Nisini, B., Benedettini, M., Pezzuto, S., Strafella, F., Barlow, M., Clegg, P. E., Cohen, M., di Giorgio, A. M., Liseau, R., Molinari, S., Palla, F., Saraceno, P., Smith, H. A., Spinoglio, L., & White, G. J. 1999, *A&A*, 346, 604

Maheswar, G., Manoj, P., & Bhatt, H. C. 2002, *A&A*, 387, 1003

Makishima, K., Tashiro, M., Ebisawa, K., Ezawa, H., Fukazawa, Y., Gunji, S., Hirayama, M., Idesawa, E., Ikebe, Y., Ishida, M., Ishisaki, Y., Iyomoto, N., Kamae, T., Kaneda, H., Kikuchi, K., Kohmura, Y., Kubo, H., Matsushita, K., Matsuzaki, K., Mihara, T., Nakagawa, K., Ohashi, T., Saito, Y., Sekimoto, Y., Takahashi, T., Tamura, T., Tsuru, T., Ueda, Y., & Yamasaki, N. Y. 1996, *PASJ*, 48, 171

Mewe, R., Kaastra, J. S., & Liedahl, D. A. 1995, *Legacy*, 6, 16

Montmerle, T., Grosso, N., Tsuboi, Y., & Koyama, K. 2000, *ApJ*, 532, 1097

Mundt, R., & Ray, T. P. 1994, in *ASP Conf. Ser.* 62: The Nature and Evolutionary Status of Herbig Ae/Be Stars, 237

Nisini, B., Milillo, A., Saraceno, P., & Vitali, F. 1995, *A&A*, 302, 169

Ohashi, T., Ebisawa, K., Fukazawa, Y., Hiyoshi, K., Horii, M., Ikebe, Y., Ikeda, H., Inoue, H., Ishida, M., Ishisaki, Y., Ishizuka, T., Kamijo, S., Kaneda, H., Kohmura, Y., Makishima, K., Mihara, T., Tashiro, M., Murakami, T., Shoumura, R., Tanaka, Y., Ueda, Y., Taguchi, K., Tsuru, T., & Takeshima, T. 1996, *PASJ*, 48, 157

Ozawa, H., Nagase, F., Ueda, Y., Dotani, T., & Ishida, M. 1999, *ApJ*, 523, L81

Palla, F., & Stahler, S. W. 1990, *ApJ*, 360, L47

—. 1993, *ApJ*, 418, 414

Pezzuto, S., Strafella, F., & Lorenzetti, D. 1997, *ApJ*, 485, 290

Pirzkal, N., Spillar, E. J., & Dyck, H. M. 1997, *ApJ*, 481, 392

Poetzel, R., Mundt, R., & Ray, T. P. 1992, *A&A*, 262, 229

Praderie, F., Simon, T., Catala, C., & Boesgaard, A. M. 1986, *ApJ*, 303, 311

Pravdo, S. H., & Marshall, F. E. 1981, *ApJ*, 248, 591

Preibisch, T. 1997, *A&A*, 324, 690

—. 1998, *A&A*, 338, L25

—. 1999, *A&A*, 345, 583

Prusti, T., Natta, A., & Palla, F. 1994, *A&A*, 292, 593

Rodriguez, L. F., Moran, J. M., Ho, P. T. P., & Gottlieb, E. W. 1980, *ApJ*, 235, 845

Rosner, R., Golub, L., & Vaiana, G. S. 1985, *ARA&A*, 23, 413

Rossi, C., Errico, L., Friedjung, M., Giovannelli, F., Muratorio, G., Viotti, R., & Vittone, A. 1999, *A&AS*, 136, 95

Ryter, C. E. 1996, *Ap&SS*, 236, 285

Schmitt, J. H. M. M., & Favata, F. 1999, *Nature*, 401, 44

Siebenmorgen, R., Prusti, T., Natta, A., & Müller, T. G. 2000, *A&A*, 361, 258

Skinner, S. L., Brown, A., & Stewart, R. T. 1993, *ApJS*, 87, 217

Skinner, S. L., & Yamauchi, S. 1996, *ApJ*, 471, 987

Smith, K., Güdel, M., & Benz, A. O. 1999, *A&A*, 349, 475

Smith, M. A., Grady, C. A., Peters, G. J., & Feigelson, E. D. 1993, *ApJ*, 409, L49

Snell, R. L., & Bally, J. 1986, *ApJ*, 303, 683

Stauffer, J. R., Caillault, J. P., Gagné, M., Prosser, C. F., & Hartmann, L. W. 1994, *ApJS*, 91, 625

Stecklum, B., Eckart, A., Henning, T., & Löwe, M. 1995, *A&A*, 296, 463

Stelzer, B., & Neuhäuser, R. 2001, *A&A*, 377, 538

Stelzer, B., Neuhäuser, R., & Hambaryan, V. 2000, *A&A*, 356, 949

Strom, K. M., & Strom, S. E. 1994, *ApJ*, 424, 237

Tagliaferri, G., Covino, S., Fleming, T. A., Gagné, M., Pallavicini, R., Haardt, F., & Uchida, Y. 1997, *A&A*, 321, 850

Tanaka, Y., Inoue, H., & Holt, S. S. 1994, *PASJ*, 46, L37

Testi, L., Palla, F., & Natta, A. 1998, *A&AS*, 133, 81

—. 1999, *A&A*, 342, 515

Thé, P. S., de Winter, D., & Pérez, M. R. 1994, *A&AS*, 104, 315

Thé, P. S., Pérez, M. R., Voshchinnikov, N. V., & van den Ancker, M. E. 1996, *A&A*, 314, 233

Tjin A Djie, H. R. E., Thé, P. S., Andersen, J., Nordström, B., Finkenzeller, U., & Jankovics, I. 1989, *A&AS*, 78, 1

Tsuboi, Y., Imanishi, K., Koyama, K., Grossi, N., & Montmerle, T. 2000, *ApJ*, 532, 1089

Tsuboi, Y., Koyama, K., Murakami, H., Hayashi, M., Skinner, S., & Ueno, S. 1998, *ApJ*, 503, 894

van den Ancker, M. E., de Winter, D., & Tjin A Djie, H. R. E. 1998, *A&A*, 330, 145

van den Ancker, M. E., Thé, P. S., Tjin A Djie, H. R. E., Catala, C., de Winter, D., Blondel, P. F. C., & Waters, L. B. F. M. 1997, *A&A*, 324, L33

Waters, L. B. F. M., & Waelkens, C. 1998, *ARA&A*, 36, 233

Weintraub, D. A. 1990, *ApJS*, 74, 575

Yamashita, A., Dotani, T., Ezuka, H., Kawasaki, M., & Takahashi, K. 1999, *Nucl. Instrum. Methods Phys. Res. A*, 436, 68

Yamauchi, S., Hamaguchi, K., Koyama, K., & Murakami, H. 1998, *PASJ*, 50, 465

Yamauchi, S., Koyama, K., Sakano, M., & Okada, K. 1996, *PASJ*, 48, 719

Yoshida, S., Kogure, T., Nakano, M., Tatematsu, K., & Wiramihardja, S. D. 1992, *PASJ*, 44, 77

Zealey, W. J., Williams, P. M., Sandell, G., Taylor, K. N. R., & Ray, T. P. 1992, *A&A*, 262, 570

Zinnecker, H., & Preibisch, T. 1994, *A&A*, 292, 152

Table 1. Stellar Parameters

Object	R.A. (2000)			Dec. (2000)			d	Sp. T	log $T_{\text{eff}}$	log $L_{\text{bol}}$	$A_V$	$v_{\text{wind}}$	$v_{\text{rot}} \sin i$
	(h	m	s)	( $^{\circ}$	'	"	(pc)		(K)	( $L_{\odot}$ )		(km s $^{-1}$ )	(km s $^{-1}$ )
BD +30 549	3	29	19.8	31	24	57	350	B8	4.08	1.1	1.9	...	...
V892 Tau	4	18	40.6	28	19	17	160	A6	...	...	4.1	250	...
AB Aur	4	55	45.8	30	33	4	144	A0	3.98	1.7	0.5	260	140
V372 Ori	5	34	47.0	−5	34	15	460 <sup>a</sup>	B9.5+A0.5	3.93	2.2	0.5	...	125
HD 36939	5	34	55.3	−5	30	22	460 <sup>a</sup>	B8−9	4.05	1.9	0.5	...	275
HD 245185	5	35	9.6	10	1	52	400	A2	3.96	1.3	0.1	...	150
LP Ori	5	35	9.8	−5	27	53	460 <sup>a</sup>	B2	4.29	3.1	0.7	...	100
MR Ori	5	35	17.0	−5	21	46	460 <sup>a</sup>	A2	3.93	1.9	1.6	...	...
V361 Ori	5	35	31.4	−5	25	16	460 <sup>a</sup>	B1.5 or B4	4.14	2.6	0.4	...	50
T Ori	5	35	50.0	−5	28	42	460	A3	3.93	1.6	1.1	...	100
V380 Ori	5	36	25.4	−6	42	58	460	B9−A0	3.97	1.9	1.4	260	200
BF Ori	5	37	13.3	−6	35	1	430	A5−6	3.90	0.1	0.3	...	100
MWC 120	5	41	2.3	−2	43	1	500	A2	3.95	1.3	0.03	...	120
VY Mon	6	31	7.0	10	26	5	800	O9−B8	4.05	2.9	7.4	...	...
VY Mon G2 <sup>b</sup>	6	31	8.2	10	26	1	800	A0	(3.99)	4.0	1.6	...	...
V590 Mon	6	40	41.3	9	48	1	800	B7	4.09	2.6	0.6	...	...
LkH $\alpha$ 218	7	2	42.3	−11	26	10	1150	B9	4.03	2.1	1.5	...	...
Z CMa	7	3	43.2	−11	33	6	1150	F6	3.80	3.4	2.8	...	<130
LkH $\alpha$ 220	7	4	5.4	−11	26	0	1150	B5	4.19	2.4	...	...	...
HD 76534	8	55	8.7	−43	28	0	830	B2	4.34	3.9	1.2	...	110
HD 97048	11	8	3.3	−77	39	17	180	B9−A0	4.00	1.6	1.2	...	140
HD 97300	11	9	50.0	−76	36	48	188	B9	(4.03)	1.5	1.3	...	...
HD 104237	12	0	5.1	−78	11	35	116	A4	3.93	1.6	0.3	500	...
IRAS 12496−7650	12	53	16.1	−77	7	2	200	A−F	(3.91)	1.7	12	...	...
HR 5999	16	8	34.3	−39	6	18	210	A5−7	3.90	1.9	0.5	100	180
HD 147889	16	25	24.3	−24	27	57	140	B2	4.34	3.3	3.3	...	...
Hen 3−1191	16	27	14.2	−48	39	28	...	B0	...	...	...	...	...
V921 Sco	16	59	6.9	−42	42	8	500	B4−5	(4.14)	3.0	7.1	500	...
MWC 297	18	27	39.6	−3	49	52	250	B1.5	(4.38)	4.5	8	380	350
HD 176386	19	1	38.9	−36	53	27	122	B9	4.03	1.7	0.6	...	...
TY CrA	19	1	40.8	−36	52	34	130	B7−9	(4.07)	1.8	1.0	...	10
R CrA	19	1	53.7	−36	57	8	130	B8	(4.06)	2.1	1.9	...	...
T CrA	19	1	59.0	−36	58	0	130	F0	(3.86)	0.9	1.7	...	40
HD 200775	21	1	36.9	68	9	48	429	B2.5	4.31	3.9	1.9	280	60
MWC 1080	23	17	26.1	60	50	43	2200	A0−3	(3.96)	3.9	4.4	400	200
EC 95	18	29	57.9	1	12	47	310	K0−K4	(3.65)	1.8	36	...	...

Note. — Sp.T: spectral type,  $T_{\text{eff}}$ : parentheses show average temperature of their spectral type. References— van den Ancker et al. (1997, 1998), Thé et al. (1994), Preibisch (1998), Nisini et al. (1995), Benedettini et al. (1998), Grady et al. (1993), Böhm & Catala (1995), Drew et al. (1997), Casey et al. (1998), van den Ancker et al. (1998), Corporon & Lagrange (1999).

<sup>a</sup>distance to the Ori OB1 association

<sup>b</sup>We refer the relative position from VY Mon to Weintraub (1990).

Table 2. *ASCA* Observation Log

Seq. ID	Abbreviation	Date	Ontime (ksec)	SIS Mode	Exposure	
					SIS (ksec)	GIS (ksec)
23021000	SVS13	1995 Aug 30	211.0	...	...	93.0
23009000	IC359	1995 Sep 2	104.6	4F/B LD 0.55	27.4	37.8
23042000	SU Aur	1995 Feb 25	114.5	2F/B	40.8	45.0
20004000	Ori Trap1	1993 Aug 30	51.4	4F/B	19.3	18.0
21005000	L1641N	1994 Mar 13	97.5	...	...	34.6
21025000	Lamb Ori	1994 Mar 12	51.3	2/1F	21.8	22.4
23019000	Ori OB1	1995 Oct 4	79.8	...	...	28.6
26007000	PSRJ0631	1998 Oct 16	157.2	...	...	81.6
25015000	15 Mon	1997 Oct 18	96.9	1F LD 0.48	36.6	36.1
23014000	Z CMa	1995 Mar 31	79.6	1F	30.5	37.6
55030000	Vela Shrap	1997 May 9	39.6	...	...	12.3
21009000	ChamI I	1994 May 14	39.3	4F/B	8.5	15.2
27017000	ChamI V	1999 Aug 7	258.9	2F	82.4	75.0
23003000	HD104237	1995 Apr 3	67.6	1F	29.9	27.1
24000000	ChamII	1996 Mar 10	69.1	...	...	24.9
24008000	Lupus3	1996 Feb 22	97.6	4F/B LD 0.7	18.2	41.3
20015010	Rho-Oph	1993 Aug 20	73.6	...	...	41.1
55003060	Gal R 1	1997 Sep 3	31.9	...	...	9.7
54004020	Gal R 2	1996 Aug 31	27.6	4F/B	12.2	11.8
21007000	MWC297 1	1994 Apr 8	49.9	1F	10.5	10.3
21007010	MWC297 2	1994 Apr 12	24.9	1F	5.3	5.0
21007020	MWC297 3	1994 Apr 12	45.4	1F	12.9	12.3
21001000	R Cra 1	1994 Apr 4	90.3	4F/B	38.4	39.4
21002000	R Cra 2	1994 Apr 8	97.5	4F/B	35.5	36.9
24016000	R Cra 3	1996 Apr 5	160.2	1F	65.2	48.8
24016010	R Cra 4	1996 Oct 18	30.8	1F	10.6	11.7
66017000	R Cra 5	1998 Apr 19	57.6	1F	17.1	16.2
26018000	R Cra 6	1998 Oct 19	108.3	1F	31.5	34.1
23029000	HD200775	1995 Nov 17	110.0	1F LD 0.55	46.0	48.7
21006000	MWC1080	1993 Dec 8	86.0	1F	36.1	38.4
25021000	Serp	1997 Apr 13	246.2	4F LD 0.7	87.4	89.9

Note. — Ontime: duration of observations, SIS Mode: number of CCD chips working (4/2/1), Data Format (Faint/Bright), Level Discri (Unit keV), Left values on slashes are CCD modes during the high telemetry mode and right values are modes during the medium and low telemetry modes.

Table 3. *ROSAT* Data Log

Object	Obs ID	Date	Exp. (ksec)	Detector	Usage
HD 245185	RH202047N00	1995 Mar 16	9.4	HRI	U
BF Ori	RH900010A01	1992 Mar 14	4.8	HRI	U
MWC 120	RP900189N00	1991 Sep 19	24.2	PSPC	U
VY Mon	RP900355N00	1992 Oct 6	5.6	PSPC	ID
	RP900355A01	1993 Mar 14	4.6	PSPC	ID
	RP900355A02	1993 Sep 16	5.4	PSPC	ID
	RP900355A03	1994 Mar 29	5.1	PSPC	ID
V590 Mon	RH200130A00	1991 Mar 20	19.6	HRI	U
LkH $\alpha$ 218	RP201011N00	1993 Apr 22	19.7	PSPC	U
LkH $\alpha$ 220	RH202153N00	1996 Apr 6	33.5	HRI	U
MWC 297	RH202048N00	1995 Sep 28	1.1	HRI	ID
HD 200775	RH202319N00	1997 Aug 11	4.8	HRI	ID

Note. — U: used for upper limit measurement (See also Table 6). ID: used for source identification.

Table 4. Selected Regions

Object	Det.	Region	
		Source	Background
V892 Tau	S	c(3) <sup>a</sup>	sym V1023 Tau
V380 Ori	G	c(3)	a(3/6)
VY Mon	G	e(4.5/2.5)	<i>sf</i> (sym optical axis)
HD 104237	S	c(2.5)	whole chip excluding <i>sr</i>
	G	c(3)	a(3/6)
IRAS 12496–7650	G	c(3)	a(3/6)
HR 5999	S	e(0.66/0.25)	sym HR 6000
V921 Sco	G	c(3)	a(3/6)
MWC 297	S	c(3)	a(3/4.4)
	G	c(3)	a(3/6)
TY CrA	S	e(0.74/0.53)	sym HD 176386
HD 176386	S	e(0.64/0.42)	sym TY CrA
TYHD <sup>b</sup>	G	c(2.5)	sym the R CrA protostar cluster
HD 200775	S	c(2.5)	<i>sf</i>
	G	c(3)	sym the SE source
MWC 1080	S	c(2.5)	<i>sf</i>
	G	c(3)	a(3/6)
EC 95	S	c(3)	b(9/3)
	G	c(3)	a(3/6)

Note. — c(*num*): *num* arcmin radius circle centered on a target, e(*num1/num2*): ellipse with *num1* arcmin long and *num2* arcmin short axes, a(*num1/num2*): annular circle with *num1* arcmin inner and *num2* arcmin outer radii, b(*num1/num2*): *num1* arcmin  $\times$  *num2* arcmin box, sym *sth*: symmetrical region with respect to *sth*, *sr*: source region, *sf*: source free region

<sup>a</sup>Including V410 X-ray 7

<sup>b</sup>GIS data merged with TY CrA and HD 176386

Table 5. *ASCA* Detected Sources

Object	Obs. ID	Detected Position							Net Count				
		R.A. (2000) (h m s)			Dec. (2000) (° ' '')			Det.	SIS (cnts)		GIS (cnts)		Total (cnts)
									(%)	(%)			
V892 Tau	IC359	4	18	39.8	28	19	16	S	722	(59)	...	( ... )	722
V380 Ori	L1641N	5	36	23.8	-6	43	18	G2	...	( ... )	109 <sup>b</sup>	(33)	109
VY Mon (/G2)	PSRJ0631	6	31	3.1	10	26	46	G	...	( ... )	338	(36)	338
HD 104237	HD104237	12	0	6.2	-78	11	29	S	2427	(84)	916	(74)	3343
IRAS 12496–7650	ChamII	12	53	16.5	-77	7	6	G	...	( ... )	100	(31)	100
HR 5999	Lupus3	16	8	34.9	-39	6	12	S	143	(48)	...	( ... )	143
V921 Sco	Gal R 2	16	59	8.7	-42	42	30	G	...	( ... )	151	(38)	151
MWC 297	MWC297 1	18	27	37.9	-3	49	36	S	353	(62)	257	(67)	610
	MWC297 2								1023	(79)	904	(87)	1927
	MWC297 3								528	(64)	349	(70)	877
TY CrA	R CrA 1	19	1	40.8	-36	52	31	S	524	(67)	...	( ... )	524
	R CrA 4								75 <sup>a</sup>	(56)	...	( ... )	75
	R CrA 6								437	(71)	...	( ... )	437
HD 176386	R CrA 1	19	1	38.7	-36	53	18	S	227	(49)	...	( ... )	227
	R CrA 4								45 <sup>a</sup>	(52)	...	( ... )	45
	R CrA 6								228	(49)	...	( ... )	228
TYHD	R CrA 1								...	( ... )	1488	(78)	1488
	R CrA 2								...	( ... )	676	(64)	676
	R CrA 3								...	( ... )	1585 <sup>c</sup>	(78)	1585
	R CrA 4								...	( ... )	510	(73)	510
	R CrA 5								...	( ... )	543	(91)	543
	R CrA 6								...	( ... )	1029	(68)	1029
HD 200775	HD200775	21	1	34.9	68	10	1	S	3361	(85)	1641	(69)	5002
MWC 1080	MWC1080	23	17	24.0	60	50	43	S	273	(33)	185	(27)	458
EC 95	Serp	18	29	58.3	1	12	43	S	3216	(75)	3679	(70)	6895

Note. — Det.: detectors measuring source positions (S: SIS, G: GIS), Net Count: background subtracted source counts, Parentheses: source event ratio defined as “source counts / (source + background) counts”, Total: net counts of SIS + GIS, TYHD: GIS data merged with TY CrA and HD 176386.

<sup>a</sup>s0 data

<sup>b</sup>g2 data

<sup>c</sup>g3 data

Table 6. *ASCA* Non-detected Sources

Object	<i>ASCA</i>					<i>ROSAT</i>				
	Obs. ID	Flux upper limit		Det.	Log $L_X$	Note	Ref.	Flux		Log $\frac{L_X}{L_{bol}}$
		Photon	Energy					Photon	Energy	
BD +30 549	SVS13	$2.1 \cdot 10^{-2}$	$1.1 \cdot 10^{-12}$	G	<31.2	con.	1	...	...	<-4.9
AB Aur	SU Aur	$3.1 \cdot 10^{-2}$	$7.4 \cdot 10^{-13}$	S	<30.3	con.	2	...	29.5	<-5.7
V372 Ori	Ori Trap1	$3.5 \cdot 10^{-2}$	$1.3 \cdot 10^{-12}$	G	<31.5	...	3	...	30.3	<-5.5
HD 36939	Ori Trap1	$4.6 \cdot 10^{-2}$	$1.7 \cdot 10^{-12}$	G	<31.6	...	3	...	<29.9	<-5.6
HD 245185	Lamb Ori	$1.6 \cdot 10^{-2}$	$3.3 \cdot 10^{-13}$	S	<30.8	...	4	$<2.4 \cdot 10^{-3}$	$<9.7 \cdot 10^{-14}$	<30.3
LP Ori	Ori Trap1	$3.6 \cdot 10^{-1}$	$9.2 \cdot 10^{-12}$	S	<32.4	con.	3	...	30.1	<-6.6
MR Ori	Ori Trap1	2.7	$9.4 \cdot 10^{-11}$	S	<33.4	con.	3	...	<29.9	<-5.2
V361 Ori	Ori Trap1	$9.8 \cdot 10^{-1}$	$2.3 \cdot 10^{-11}$	S	<32.8	con.	3	...	30.9	<-5.4
T Ori	Ori Trap1	$6.5 \cdot 10^{-2}$	$1.6 \cdot 10^{-12}$	S	<31.6	con.	3	...	29.9	<-5.3
BF Ori	L1641N	...	$5.8 \cdot 10^{-13}$	G	<31.1	ano.	4	$<2.2 \cdot 10^{-3}$	$<6.7 \cdot 10^{-14}$	<30.2
MWC 120	Ori OB1	$9.5 \cdot 10^{-3}$	$3.1 \cdot 10^{-13}$	G	<31.0	...	4	$<2.7 \cdot 10^{-3}$	$<3.3 \cdot 10^{-14}$	<30.0
V590 Mon	15 Mon	$4.8 \cdot 10^{-2}$	$1.2 \cdot 10^{-12}$	S	<32.0	...	4	$4.2 \cdot 10^{-3}$	$2.4 \cdot 10^{-13}$	31.3
LkH $\alpha$ 218	Z CMa	$9.9 \cdot 10^{-2}$	$4.4 \cdot 10^{-12}$	G	<32.8	...	4	$<3.7 \cdot 10^{-2}$	$<1.2 \cdot 10^{-12}$	<32.3
Z CMa	Z CMa	$1.9 \cdot 10^{-2}$	$8.9 \cdot 10^{-13}$	S	<32.1	...	2	...	31.1	<-5.8
LkH $\alpha$ 220	Z CMa	$8.5 \cdot 10^{-3}$	$2.8 \cdot 10^{-13}\dagger$	G	<31.6	con.	4	$<7.0 \cdot 10^{-4}$	$<2.2 \cdot 10^{-14}$	<30.5
HD 76534	Vela Shrap	$1.0 \cdot 10^{-2}$	$4.3 \cdot 10^{-13}$	G	<31.6	...	5	...	...	<-5.9
HD 97048	ChamI V	...	$1.8 \cdot 10^{-13}$	S	<29.8	ano.	2	...	29.0	<-6.2
HD 97300	ChamI I	$5.1 \cdot 10^{-2}$	$2.3 \cdot 10^{-12}$	G	<31.0	con.	6	...	29.0	<-6.1
HD 147889	Rho-Oph	...	$1.7 \cdot 10^{-12}$	G	<30.6	ano.	7	...	<27.5	<-9.4
Hen 3-1191	Gal R 1	$2.3 \cdot 10^{-2}$	$7.5 \cdot 10^{-13}\dagger$	G	...	...	5	...	...	...
R CrA	R CrA 1	$1.4 \cdot 10^{-1}$	$5.2 \cdot 10^{-12}$	S	<31.0	con.	2	...	<28.7	<-7.0
T CrA	R CrA 1	$4.0 \cdot 10^{-2}$	$1.5 \cdot 10^{-12}$	S	<30.5	con.	2	...	<28.5	<-6.0

Note. — The column of *ASCA*, flux upper limit (0.5–10 keV), Photon [cnts s $^{-1}$ ]: 3 $\sigma$  level or count rate of source contamination estimated from a 40'' and 80'' square regions for the SIS and GIS, respectively. Energy [ergs cm $^{-2}$  s $^{-1}$ ]: unabsorbed energy flux upperlimit calculated using the PIMMS package, assuming thin-thermal plasma with  $kT \sim 2$  keV and  $N_H$  converted from the  $A_V$ , Log  $L_X$  [ergs s $^{-1}$ ] (0.5–10 keV): absorption corrected X-ray luminosity, Det.: detectors measuring count rates (S: SIS, G: GIS), Sources marked as “con.” have source contamination, Sources marked as “ano.” are identified as the other objects.  $\dagger$  assuming no absorption ( $N_H = 0.0$  cm $^{-2}$ ). The column of *ROSAT*, ref.: reference of log  $L_X$ , 1: Preibisch (1997), 2: Zinnecker & Preibisch (1994), 3: Gagné et al. (1995), 4: this work, 5: no pointing observation, 6: Feigelson et al. (1993), 7: Casanova et al. (1995), Flux (0.1–2.4 keV): Photon [cnts s $^{-1}$ ], Energy [ergs cm $^{-2}$  s $^{-1}$ ], absorption corrected energy flux assuming thin-thermal plasma of  $kT \sim 2$  keV and  $N_H$  converted from  $A_V$ , Log  $L_X$  [ergs s $^{-1}$ ] (0.1–2.4 keV): absorption corrected X-ray luminosity. Sources marked as “con.” have source contamination.

Table 7. Result of *ASCA* Timing Analysis

Object	St.	Det.	Bin	Constant Fittings			
				Mean (sec)	Mean (cnts s <sup>-1</sup> )	Reduced $\chi^2(d.o.f)$	Var.
V892 Tau		S	2048	$1.5 \cdot 10^{-2}$	1.42	(27)	n
V380 Ori		G2	2048	$2.4 \cdot 10^{-3}$	0.94	(33)	n
VY Mon (/G2)		G	2048	$8.9 \cdot 10^{-3}$	1.69	(70)	y
HD 104237		SG	2048	$2.8 \cdot 10^{-2}$	2.62	(31)	y
IRAS 12496–7650		G	2048	$1.6 \cdot 10^{-3}$	1.00	(30)	n
HR 5999		S	2048	$3.4 \cdot 10^{-3}$	1.08	(21)	n
V921 Sco		G	2048	$6.3 \cdot 10^{-3}$	0.51	(11)	n
MWC 297	1	SG	2048	$1.5 \cdot 10^{-2}$	0.25	(10)	n
	2	SG	2048	$9.0 \cdot 10^{-2}$	4.51	(7)	y
	3	SG	2048	$1.6 \cdot 10^{-2}$	4.56	(13)	y
TY CrA	1	S	2048	$6.4 \cdot 10^{-3}$	0.79	(34)	n
	4	S	2048	$5.8 \cdot 10^{-3}$	1.09	(12)	n
	6	S	2048	$6.7 \cdot 10^{-3}$	0.90	(39)	n
HD 176386	1	S	2048	$2.8 \cdot 10^{-3}$	0.83	(33)	n
	4	S	2048	$4.4 \cdot 10^{-3}$	0.40	(12)	n
	6	S	2048	$2.1 \cdot 10^{-3}$	1.21	(39)	n
TYHD	1	G	2048	$1.4 \cdot 10^{-2}$	1.67	(36)	y
	2	G	2048	$1.3 \cdot 10^{-2}$	1.42	(37)	n
	3	G	4096	$4.0 \cdot 10^{-2}$	3.14	(33)	y
	4	G	2048	$1.5 \cdot 10^{-2}$	1.79	(14)	n
	5	G	2048	$1.8 \cdot 10^{-2}$	0.84	(21)	n
	6	G	2048	$6.7 \cdot 10^{-3}$	0.90	(39)	n
HD 200775	S1G <sup>a</sup>	2048		$2.1 \cdot 10^{-2}$	1.71	(47)	y
MWC 1080	SG	4096		$3.0 \cdot 10^{-3}$	0.79	(19)	n
EC 95	SG	2048		$1.7 \cdot 10^{-2}$	2.28	(92)	y

Note. — St.: number of observation ID., Det.: detector (S: SIS, G: GIS, SG: SIS + GIS), Bin.: binning time scales of light curves, Mean: average count rates derived from constant fittings, Var.: sources showing time variation above 96% confidence level, TYHD: GIS data merged with TY CrA and HD 176386.

<sup>a</sup>SIS1 + GIS

Table 8. Result of *ASCA* Spectral Analysis

Object	St.	Det.	Model	<i>kT</i>	<i>E.M.</i>	<i>N<sub>H</sub></i>	Reduced $\chi^2$ ( <i>d.o.f.</i> )	Flux	<i>L<sub>X</sub></i>	<i>L<sub>X</sub></i> / <i>L<sub>bol</sub></i>	
V892 Tau	S	1T	2.0	(1.6–2.5)	54.0 (53.9–54.1)	1.2 (0.9–1.6)	0.99 (51)	1.22	...	...	
	S	2T	2.0	(fix)	54.0 (fix)	1.8 (fix)	0.87 (54)	1.02	31.0	–4.4	
V380 Ori	G2	1T	3.2	(0.7–11.0)	54.3 (53.9–55.4)	1.7 (1.2–2.8)	...	0.20	31.3 <sup>b</sup>	...	
	G2	1T <sup>F</sup>	2.4	(1.3–6.1)	54.2 (54.0–54.4)	0.3 (0.0–1.5)	1.31 (14)	0.59	31.2	–4.4	
VY Mon (/G2)	LS	G	1T	2.9	(2.0–4.6)	55.1 (55.0–55.3)	0.6 (0.2–1.0)	1.40 (42)	1.21	32.2	–5.4 <sup>d</sup>
	LS	G	1T <sup>Gc</sup>	2.2	(1.6–3.3)	55.2 (55.0–55.4)	0.8 (0.4–1.2)	1.23 (40)	1.18	32.2	–5.4 <sup>d</sup>
	HS	G	1T	6.0	(3.8–12.3)	55.2 (55.1–55.3)	0.4 (0.1–0.8)	1.29 (45)	2.49	32.4	–4.1 <sup>d</sup>
	HS	G	1T <sup>LS</sup>	20.3	(3.0–)	54.8 (54.7–55.2)	0.6 (0.0–2.5)	1.28 (45)	1.24	32.1	–4.4 <sup>d</sup>
HD 104237	SG	1T	2.1	(...	53.3 (...	0.0 (...	3.82 (89)	...	...	...	
	SG	2T	0.7	(0.6–0.7)	52.9 (52.8–53.1)	0.1 (0.0–0.2)	1.57 (87)	0.43	29.9	–5.2	
IRAS 12496–7650	G	1T	2.0	(0.9–7.2)	54.1 (53.4–55.3)	13 (6.2–24)	0.93 (14)	0.29	31.1	–4.2	
	HR 5999	S	1T	0.9	(0.6–1.7)	53.9 (53.5–54.3)	0.7 (0.0–1.2)	1.15 (11)	0.37	30.9	–4.6
V921 Sco	S	1T <sup>F</sup>	1.6	(1.2–2.4)	53.5 (53.4–53.6)	0.1 (fix)	1.27 (12)	0.44	30.4	–5.1	
	G	1T	2.8	(1.1–9.1)	55.0 (54.6–56.1)	4.9 (2.3–14)	0.96 (18)	1.14	32.1	–4.5	
MWC 297	1	SG	1T	3.4	(2.4–5.1)	54.2 (54.1–54.4)	2.4 (1.8–3.1)	0.92 (43)	1.18	31.3	–6.8
	2	SG	1T	6.5	(4.7–9.6)	54.9 (54.8–55.0)	2.5 (2.1–2.8)	1.04 (105)	9.23	32.1	–6.0
TY CrA	3	SG	1T	3.4	(2.6–4.8)	54.2 (54.1–54.3)	1.9 (1.5–2.4)	0.89 (63)	1.31	31.3	–6.7
	1	S	1T	1.8	(0.8–2.3)	53.4 (53.3–53.5)	0.3 (0.1–0.5)	1.02 (28)	0.76	30.4	–5.1
TYHD	4	S	1T <sup>F</sup>	1.8	(1.2–3.4)	53.5 (53.3–53.7)	0.4 (fix)	1.33 (5)	0.89	30.5	–4.9
	6	S	1T	1.2	(1.0–1.4)	53.7 (53.5–53.8)	0.6 (0.3–0.9)	0.87 (25)	0.82	30.6	–4.8
HD 176386	1	S	1T	1.3	(1.0–1.8)	52.8 (52.7–52.9)	0.0 (0.0–0.2)	0.90 (16)	0.32	29.8	–5.5
	4	S	1T <sup>F</sup>	1.0	(0.7–1.5)	53.0 (52.8–53.2)	0.0 (fix)	0.56 (4)	0.50	30.0	–5.3
TYHD	6	S	1T	1.9	(1.3–2.8)	52.9 (52.8–53.9)	0.0 (0.0–0.2)	1.93 (13)	0.39	29.8	–5.4
	1	G	1T	2.1	(1.9–2.4)	53.6 (53.6–53.6)	0.0 (0.0–0.1)	1.87 (26)	1.86	...	...
HD 200775	2	G	1T	1.7	(1.2–2.0)	53.6 (53.6–53.8)	0.0 (0.0–0.5)	0.66 (41)	1.74	...	...
	3LS	G3	1T	2.6	(2.1–3.1)	53.7 (53.6–53.7)	0.0 (0.0–0.1)	0.79 (65)	2.43	...	...
3HS	G3	1T	3.0	(2.4–3.8)	53.8 (53.8–53.9)	0.0 (0.0–0.2)	0.88 (22)	3.87	...	...	
	4	G	1T	2.5	(2.0–3.3)	53.6 (53.5–53.6)	0.0 (0.0–0.2)	1.18 (30)	1.92	...	...
MWC 1080	5	G	1T	2.1	(1.3–2.6)	53.7 (53.6–53.9)	0.0 (0.0–0.4)	0.98 (25)	2.26	...	...
	6	G	1T	1.7	(1.4–1.9)	53.5 (53.5–53.6)	0.0 (0.0–0.2)	1.03 (64)	1.49	...	...
EC 95	SG	1T	1.7	(1.6–1.9)	54.5 (54.5–54.6)	0.1 (0.0–0.2)	1.39 (211)	1.11	31.5	–6.0	
	SG	2T	0.5	(0.4–0.7)	55.2 (55.1–55.4)	0.9 (0.8–1.0)	1.15 (209)	0.59	32.1	–5.3	
TYHD				2.8	(1.9–3.8)	54.2 (54.1–54.5)	0.9 (com.)	...	0.47	31.3	–6.2
	SG	1T <sup>Ge</sup>	7.2	(3.0–)	55.1 (54.9–55.3)	1.0 (0.3–2.2)	0.97 (54)	0.27	32.3	–5.1	
TYHD	SG	1T	3.9	(3.5–4.4)	54.5 (54.5–54.6) <sup>f</sup>	2.3 (2.0–2.5)	1.20 (205)	1.97 <sup>f</sup>	31.7	–3.7	

Note. — St.: number of observation ID and/or status (HS: high or flare state, LS: low or quiescent state), Det.: S: SIS, G: GIS, SG: SIS+GIS, Model: 1T: 1-temperature, 2T: 2-temperature,  $G/LS$ : adding the components of Gaussian/low state,  $F$ : fixing  $N_{\text{H}}$  value,  $kT$  [keV],  $E.M.$  [log,  $\text{cm}^{-3}$ ],  $N_{\text{H}}$  [ $10^{22} \text{ cm}^{-2}$ ], com.: common  $N_{\text{H}}$  values with the above column, fix: parameter is fixed, Parentheses show 90% confidence level, Reduced  $\chi^2$ : parentheses denote number of degree of freedom (*d.o.f.*), Flux [ $10^{-12} \text{ ergs cm}^{-2} \text{ s}^{-1}$ ]: observed flux (0.5–10 keV),  $L_{\text{X}}$  [log,  $\text{ergs s}^{-1}$ ]: absorption corrected X-ray luminosity between 0.5–10 keV,  $L_{\text{X}}/L_{\text{bol}}$  [log], TYHD: GIS data merged with TY CrA and HD 176386

<sup>a</sup> $N_{\text{H}}$  is fixed in the error estimate

<sup>b</sup>the distance to V410 X-ray 7

<sup>c</sup>best-fit parameters of the Gaussian component [center energy, 5.1 (4.8–5.3) keV assuming line width of 0.0 eV.]

<sup>d</sup> $L_{\text{bol}}$  of VY Mon G2

<sup>e</sup>best-fit parameters of the Gaussian component [center energy, 6.4 (6.2–6.6) keV assuming line width of 0.0 eV.]

<sup>f</sup>GIS value

Table 9. Fitting Results of the Flare Light Curves

Object	Obs. ID	Det.	$I_{qui}$ (cnts s $^{-1}$ )	$I_{peak}$ (cnts s $^{-1}$ )	$\tau_{ris}$ (10 $^4$ sec)	$\tau_{dec}$ (10 $^4$ sec)
MWC 297	MWC297 2,3	SG	2.3 (2.1–2.4) 10 $^{-2}$	> 1.2 10 $^{-1}$ <sup>a</sup>	...	5.6 (4.5–7.0)
VY Mon	PSRJ0631	G	2.5 (1.7–2.9) 10 $^{-3}$	> 3.8 10 $^{-3}$ <sup>a</sup>	...	3.6 (2.0–7.4)
TYHD <sup>b</sup>	R CrA3	G	3.6 (3.4–3.8) 10 $^{-2}$	~ 7.5 10 $^{-2}$	~ 1	2.4 (1.3–8.0)

Note. — Det.: detector, S: SIS, G: GIS.,  $\tau_{dec}$ :  $e$ -folding time fit by a constant and exponential decay model.  $\tau_{ris}$ : the period between the constant level to the flux peak.

<sup>a</sup>count rate at the observation start.

<sup>b</sup>GIS data merged with TY CrA and HD 176386.

Table 10. Outflow Activity

$\log L_X$ (ergs s $^{-1}$ )	Outflow Activity	
	Yes	No activity found
Above 30	V380 Ori <sup>1,2</sup> , Z CMa <sup>2</sup> , IRAS 12496-7650 <sup>3,5</sup> , HD 200775 <sup>2,4</sup> , MWC 1080 <sup>2,6</sup> , EC 95 <sup>7,a</sup>	V892 Tau <sup>2</sup> , HD 104237 <sup>8</sup> , HR 5999 <sup>2</sup> , MWC297 <sup>3</sup>
Below 30	R CrA <sup>2,3</sup> , T CrA <sup>2</sup>	T Ori <sup>2</sup> , HD 76534 <sup>2</sup> , HD 97048 <sup>3</sup>

Note. — References: <sup>1</sup>Corcoran & Ray (1995), <sup>2</sup>Maheswar et al. (2002) (Table 2, column 8), <sup>3</sup>Lorenzetti et al. (1999) (Table 2, column 5), <sup>4</sup>Fuente et al. (1998), <sup>5</sup>Hughes et al. (1989), <sup>6</sup>Poetzel et al. (1992), <sup>7</sup>Eiroa & Casali (1989), <sup>8</sup>Knee & Prusti (1996). Sources with blanks in the columns of Maheswar et al. (2002) and Lorenzetti et al. (1999) are listed in "no activity found".

<sup>a</sup>proto-HAeBe

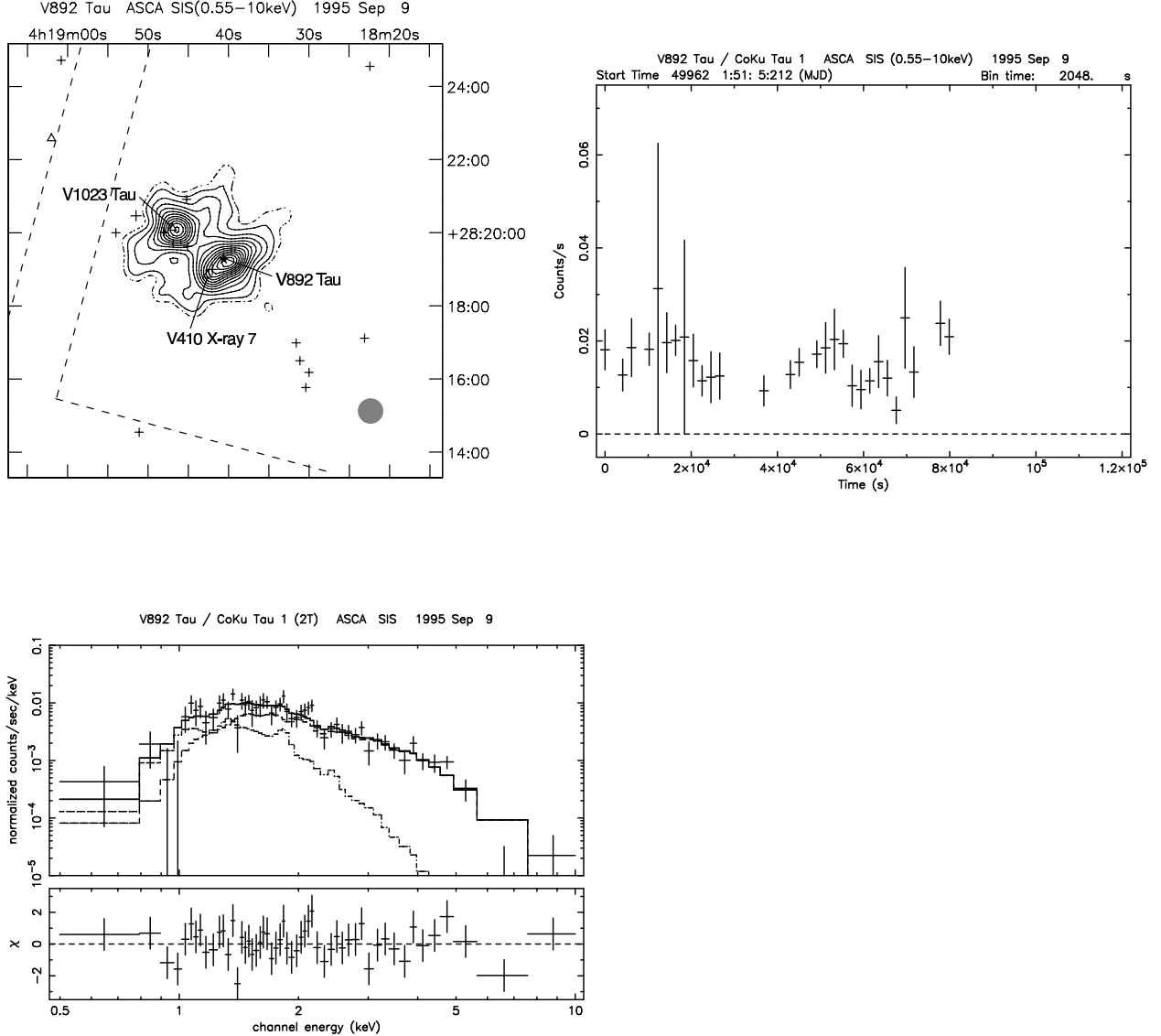


Fig. 1.— a: *ASCA* image of the V892 Tau field ( $12' \times 12'$ ) (*top left panel*). The contour image smoothed with a Gaussian function of  $\sigma \sim 2$  pixel (SIS:  $6.^{\prime\prime}4$  pixel $^{-1}$ , GIS:  $14.^{\prime\prime}7$  pixel $^{-1}$ ) is drawn by 0.4 cnts pixel $^{-1}$  for the SIS and 0.5 cnts pixel $^{-1}$  for the GIS. A dot-dash line represents  $5\sigma$  detection levels of the Poisson-distributed photon error of the background. Dash-lines are the detector rims. The filled circle on the bottom right shows the typical error circle of the SIS ( $20''$ ) and the GIS ( $40''$ ). The coordinate system is *J2000*. *Legend* – star: HAeBe, diamond: infrared source, triangle: young star and PMS object, square: radio source, cross: normal star, asterisk: galaxy. The source category is referred to the SIMBAD database. b: SIS light curves of V892 Tau (*top right panel*). The background is subtracted. The vertical axis is averaged detector count rates. Dotted lines are the zero level. 1 bin is 2,048 sec. c: SIS spectrum of V892 Tau including the component of V410 X-ray 7 (2T model in Table 8, *bottom left panel*). The solid and dotted lines show the best-fit model of the total and each component, respectively. The residual of the best-fit model is displayed in the lower section.

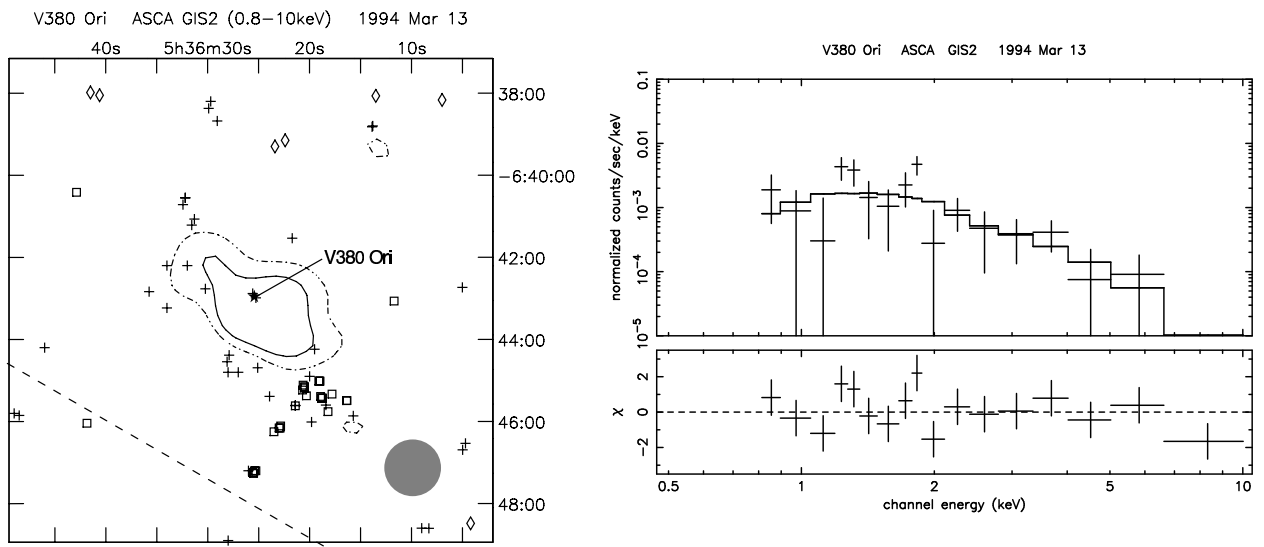


Fig. 2.— a: GIS image of the V380 Ori field (*left panel*). See Figure 1a for details. b: GIS spectrum of V380 Ori (*right panel*). See Figure 1c for details.

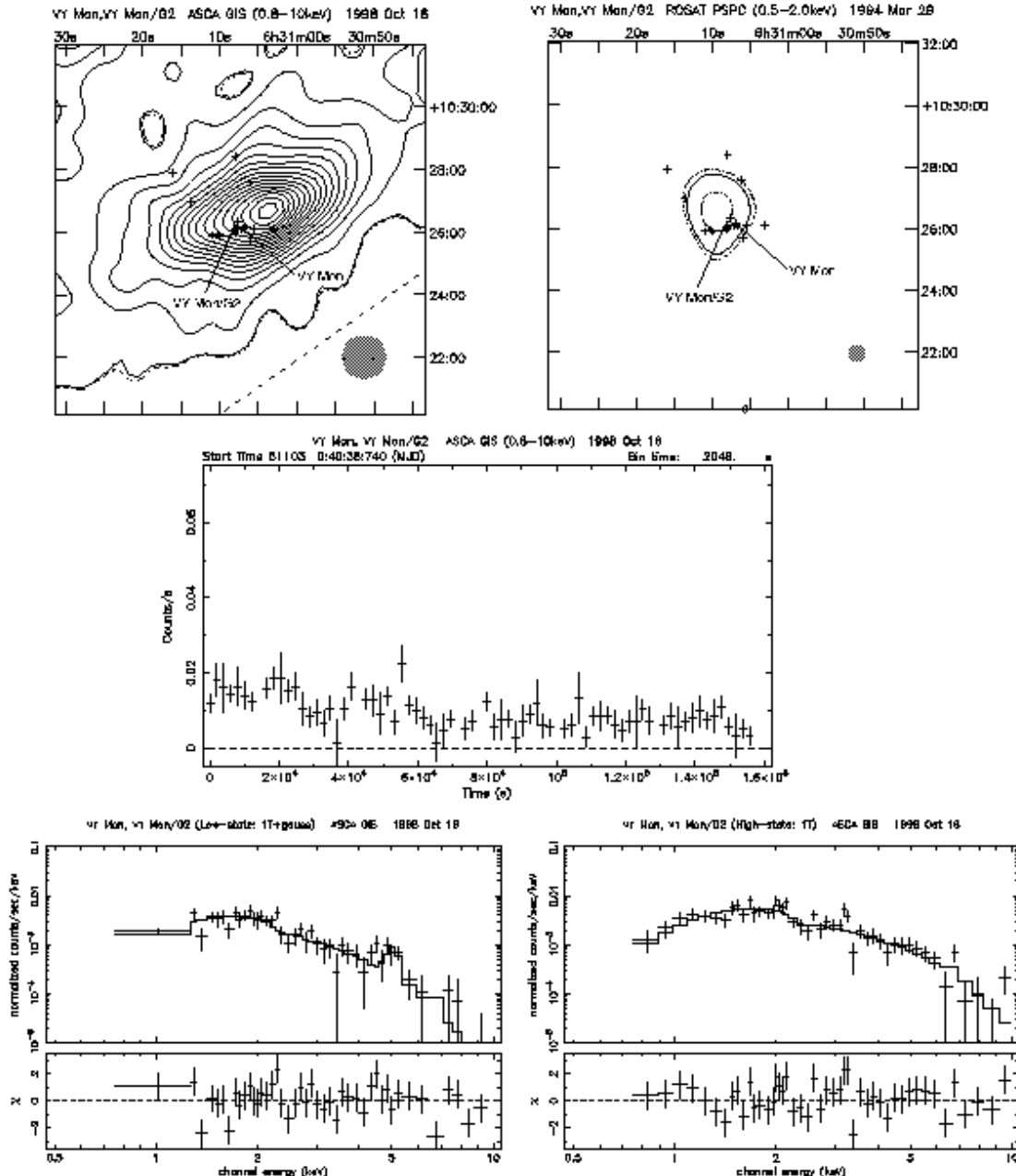


Fig. 3.— a: *ASCA* GIS image of the VY Mon field (*top left panel*) and *ROSAT* PSPC image of the VY Mon field (*top right panel*). The star marks are VY Mon (*right*) and CoKu VY Mon/G2 (*left*), respectively. b: GIS light curves of VY Mon (*middle panel*). c: GIS spectra of VY Mon (*bottom left panel*: LS, *bottom right panel*: HS).

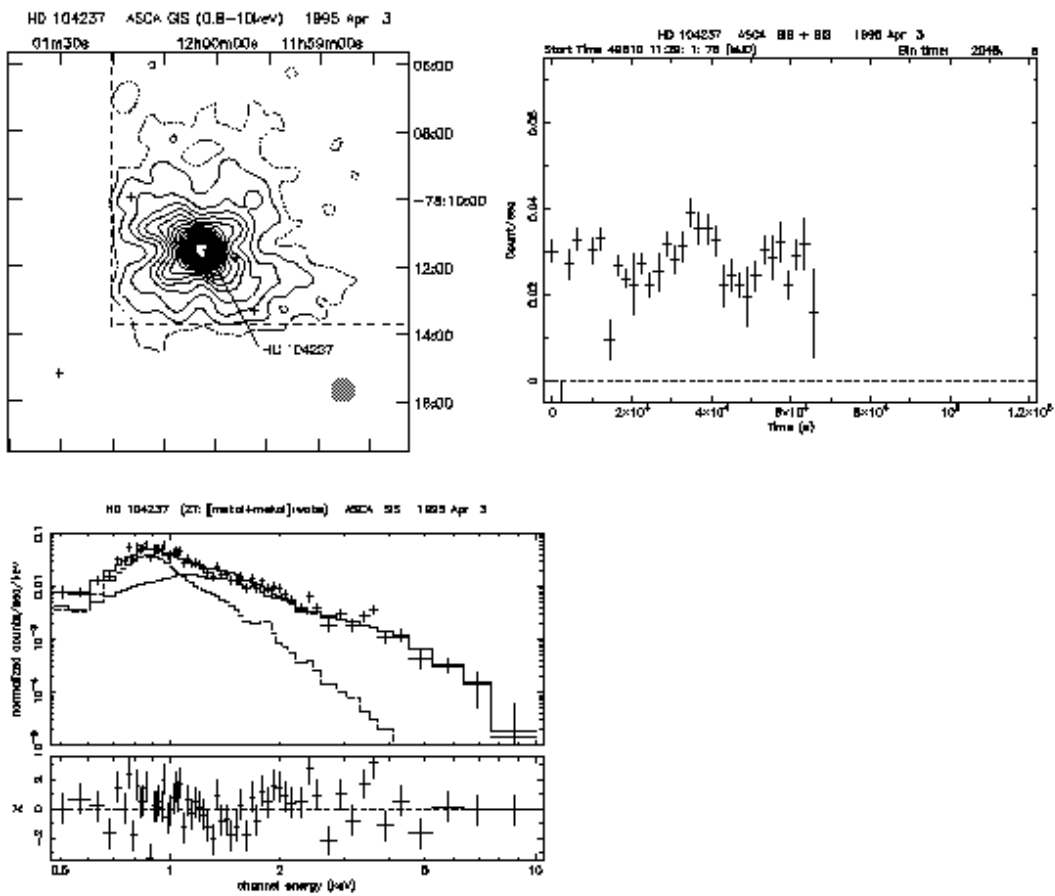


Fig. 4.— a: SIS image of HD 104237 (*top left panel*). b: Light curves of HD 104237 (*top right panel*). c: SIS spectrum of HD 104237 fit by a commonly absorbed 2T model (2T model in Table 8, *bottom left panel*).

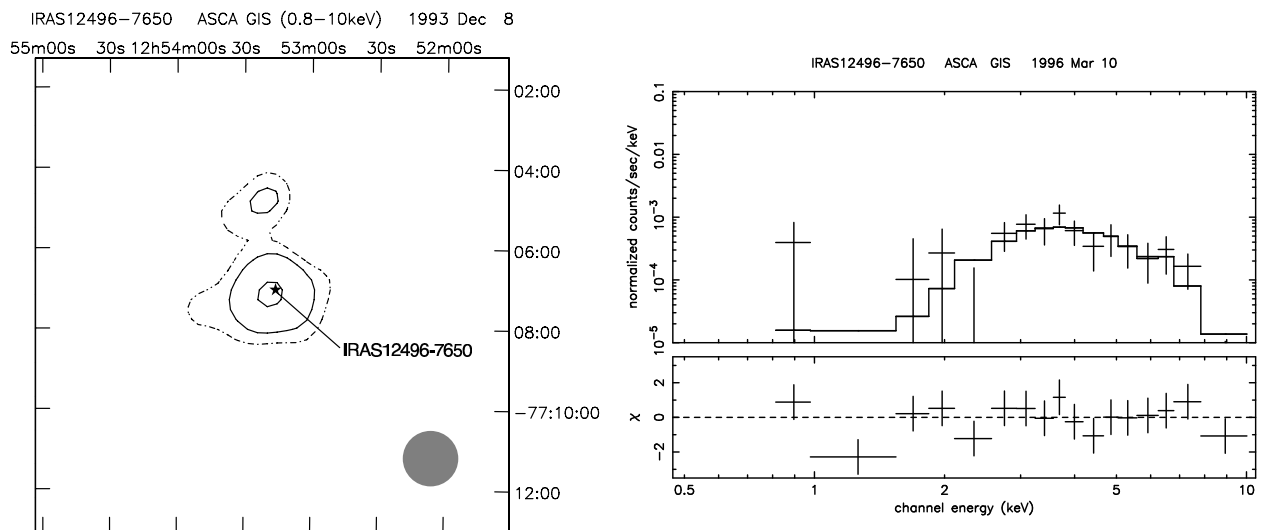


Fig. 5.— a: GIS image of IRAS 12496–7650 (*left panel*). b: GIS spectrum of IRAS 12496–7650 (*right panel*).

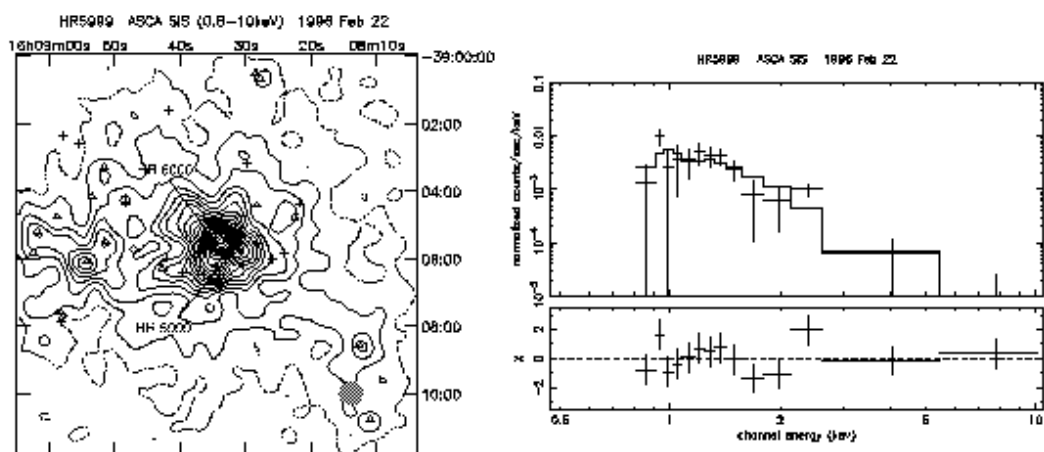


Fig. 6.— a: SIS image of HR 5999 (*left panel*). b: SIS spectrum of HR 5999 (*right panel*).

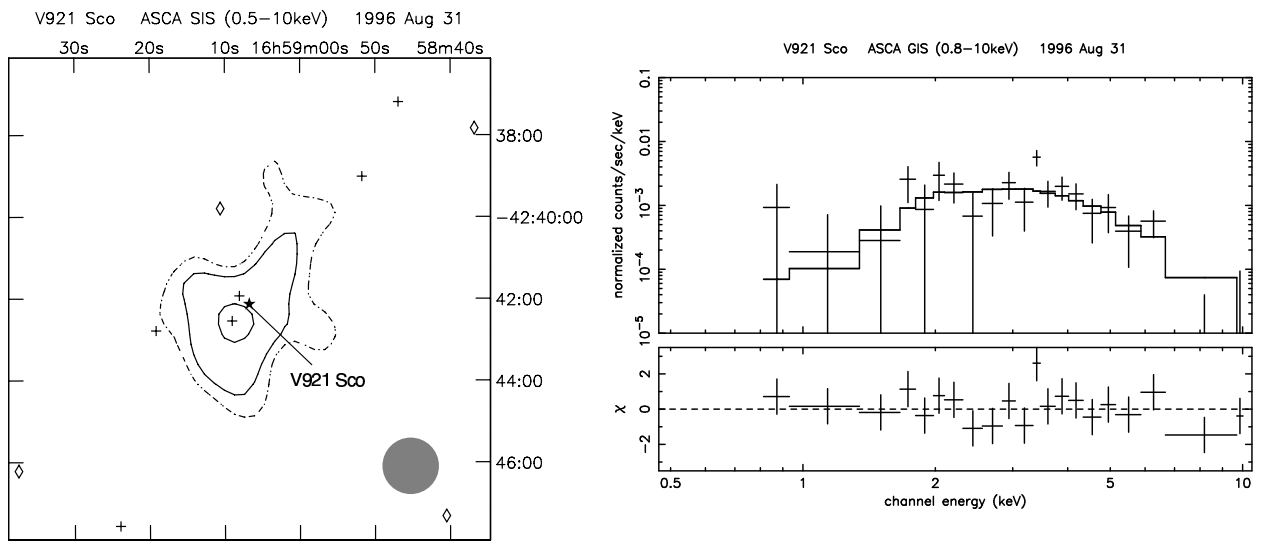


Fig. 7.— a: GIS image of V921 Sco (*left panel*). b: GIS spectrum of V921 Sco (*right panel*).

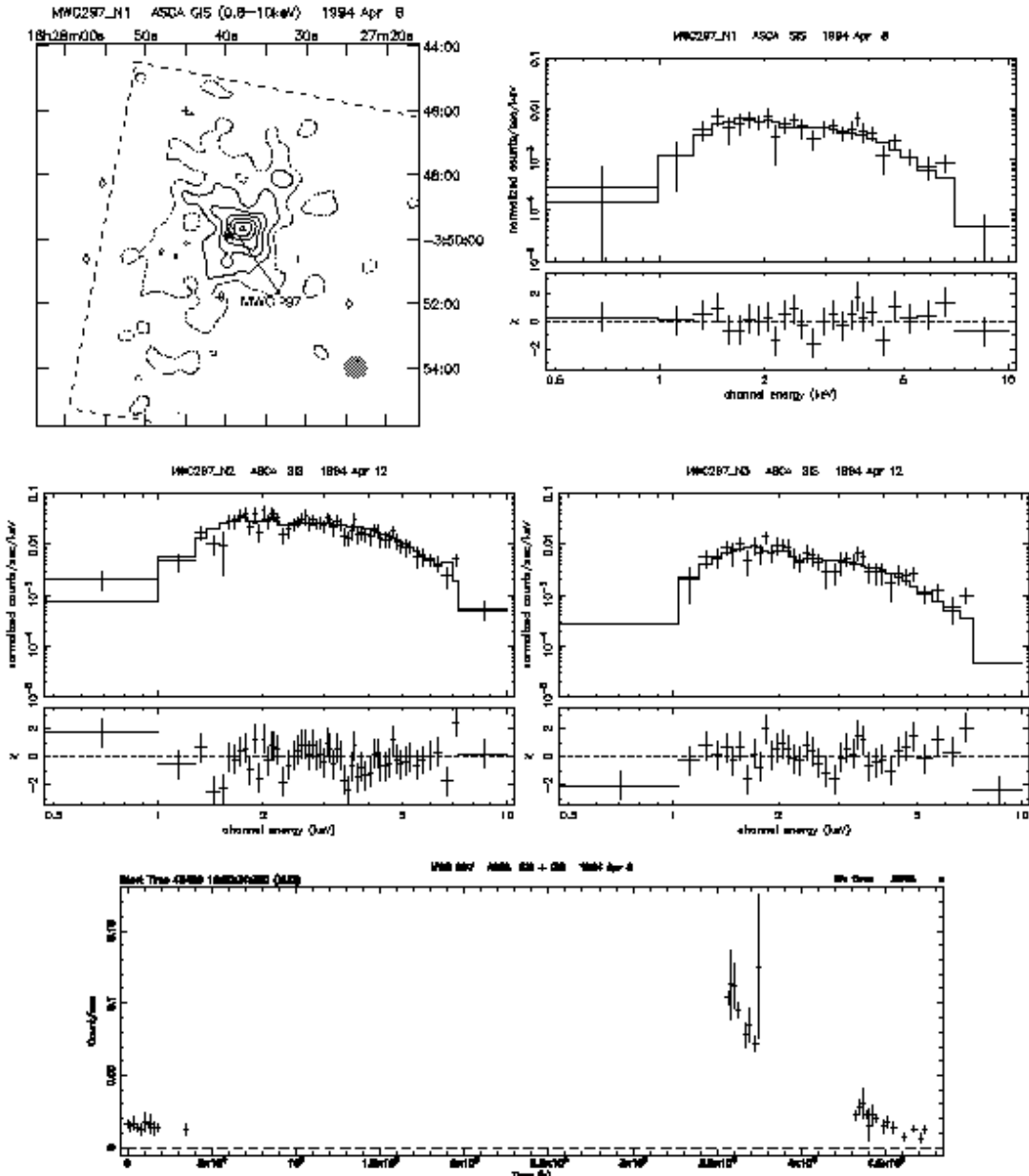


Fig. 8.— a: SIS image of the MWC 297 field in "MWC 297 1" (top left panel). The count rate per solid-line is  $0.2 \text{ cnts pixel}^{-1}$ . b: Light curve of MWC 297 (bottom panel). c: SIS spectra of MWC 297 in the "MWC297 1, 2 and 3" (top right, middle left, and middle right panels, respectively).

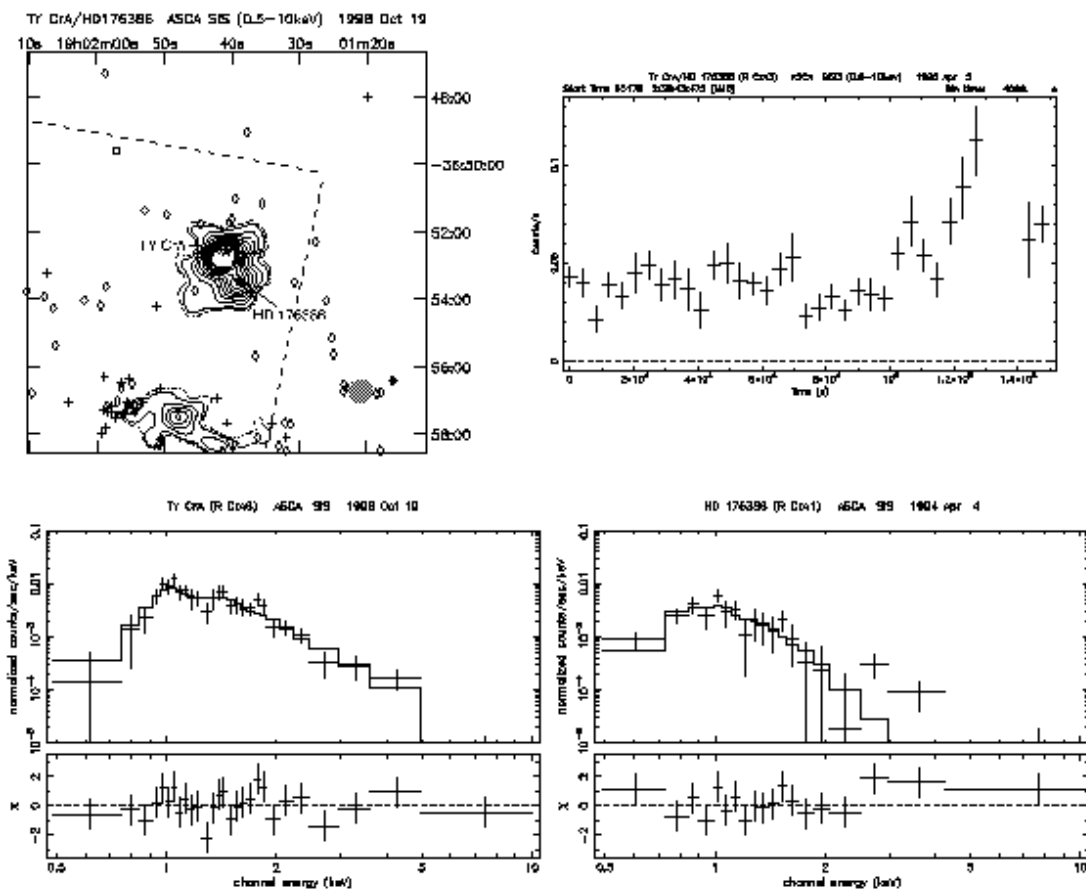


Fig. 9.— a: SIS image of the TY CrA/HD 176386 field in Oct 1998 (R CrA6, *top left panel*). b: GIS light curves of TY CrA + HD 176386 (R CrA3 *top right panel*). c: SIS spectra of TY CrA (R CrA 6, *bottom left panel*) and HD 176386 (R CrA 1, *bottom right panel*)

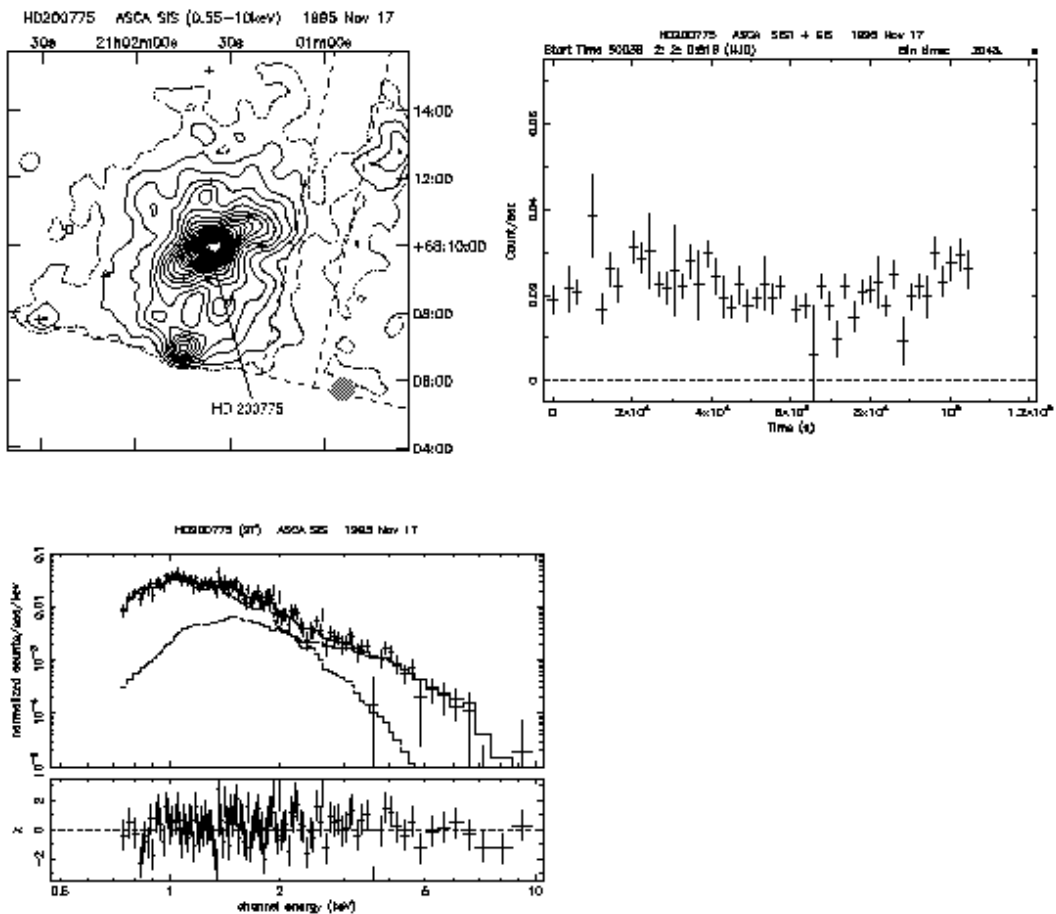


Fig. 10.— a: SIS image of HD 200775 (*top left panel*). b: Light curves (SIS1+GIS) of HD 200775 (*top right panel*). c: SIS spectrum of HD 200775 fit by an absorbed 2T model (*bottom left panel*).

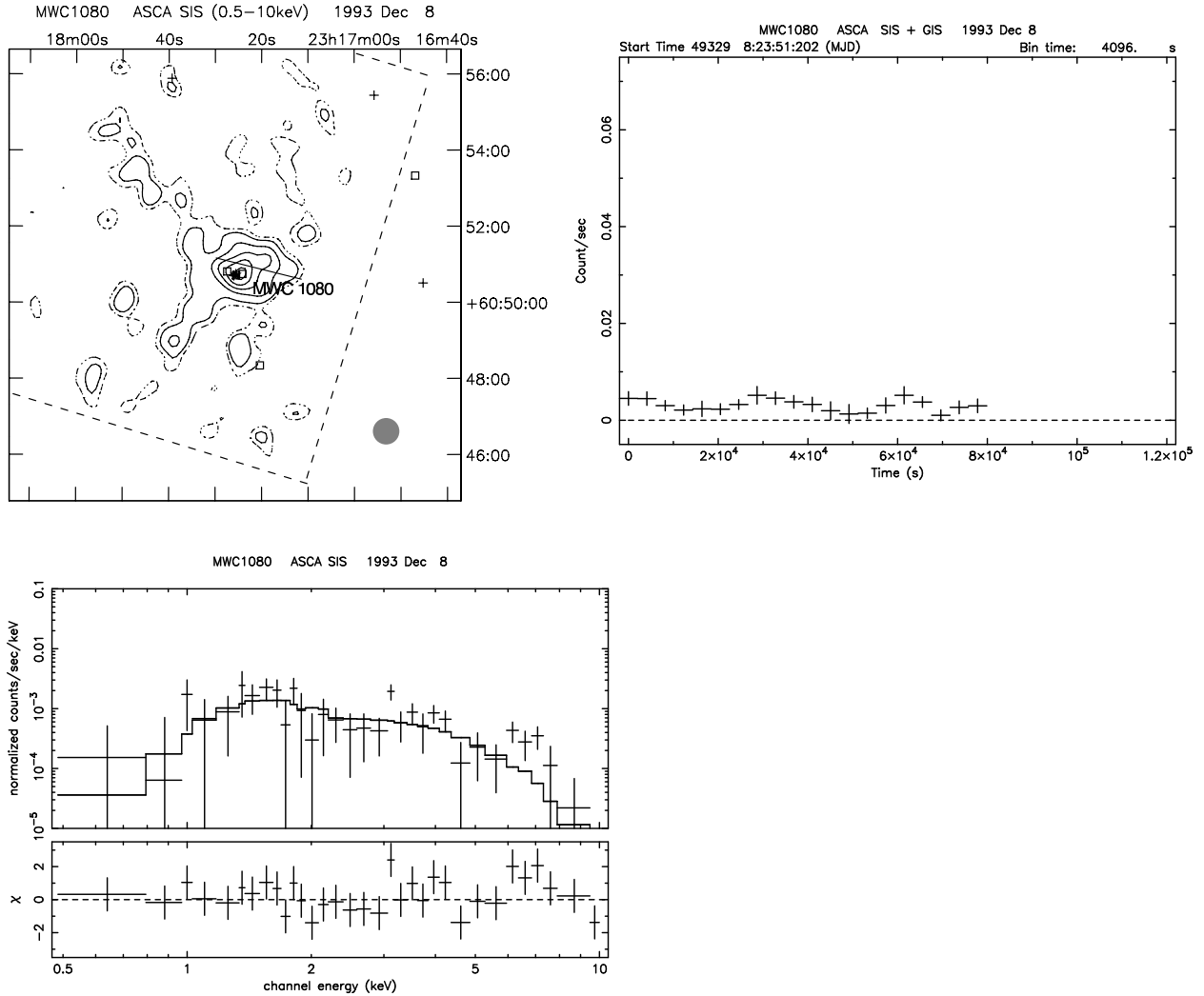


Fig. 11.— a: SIS image of MWC 1080 (*top left panel*). The count rate per solid-line is 0.2 cnts pixel<sup>-1</sup>. b: Light curves of MWC 1080 (*top right panel*). c: SIS spectrum of MWC 1080 (*bottom left panel*).

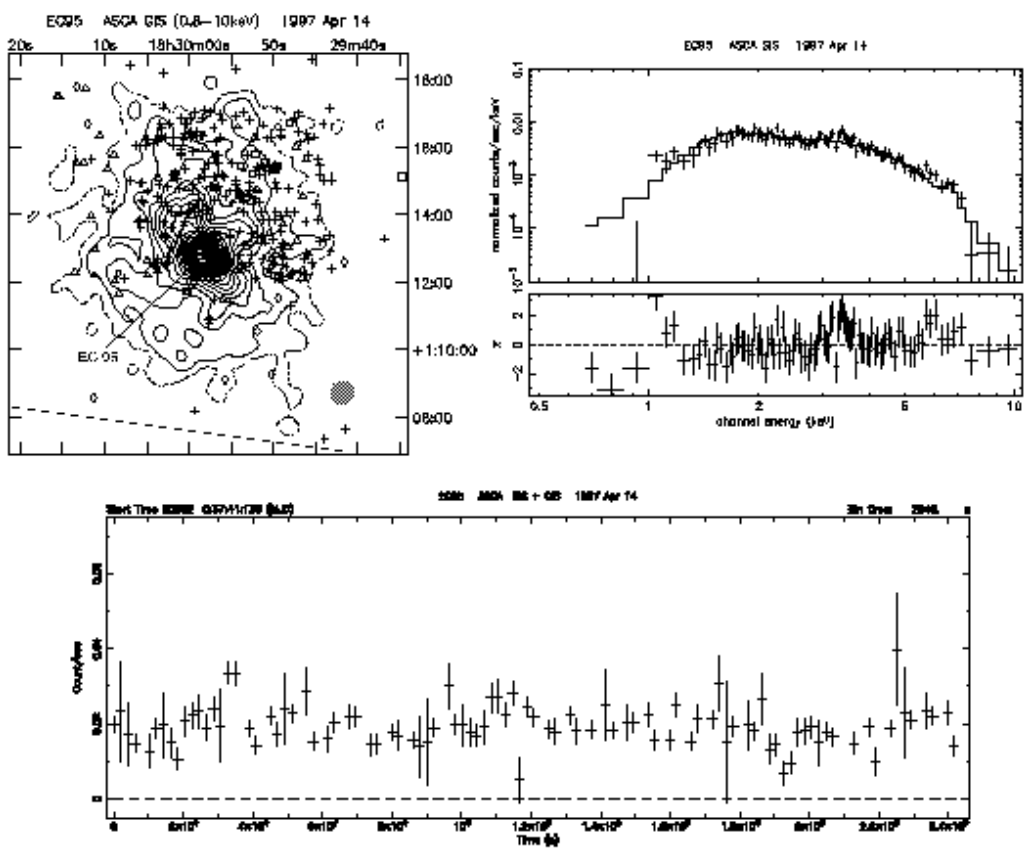


Fig. 12.— a: SIS image of the EC 95 field (*top left panel*). b: Light curves of EC 95 (*bottom panel*). c: SIS spectrum of EC 95 (*top right panel*).

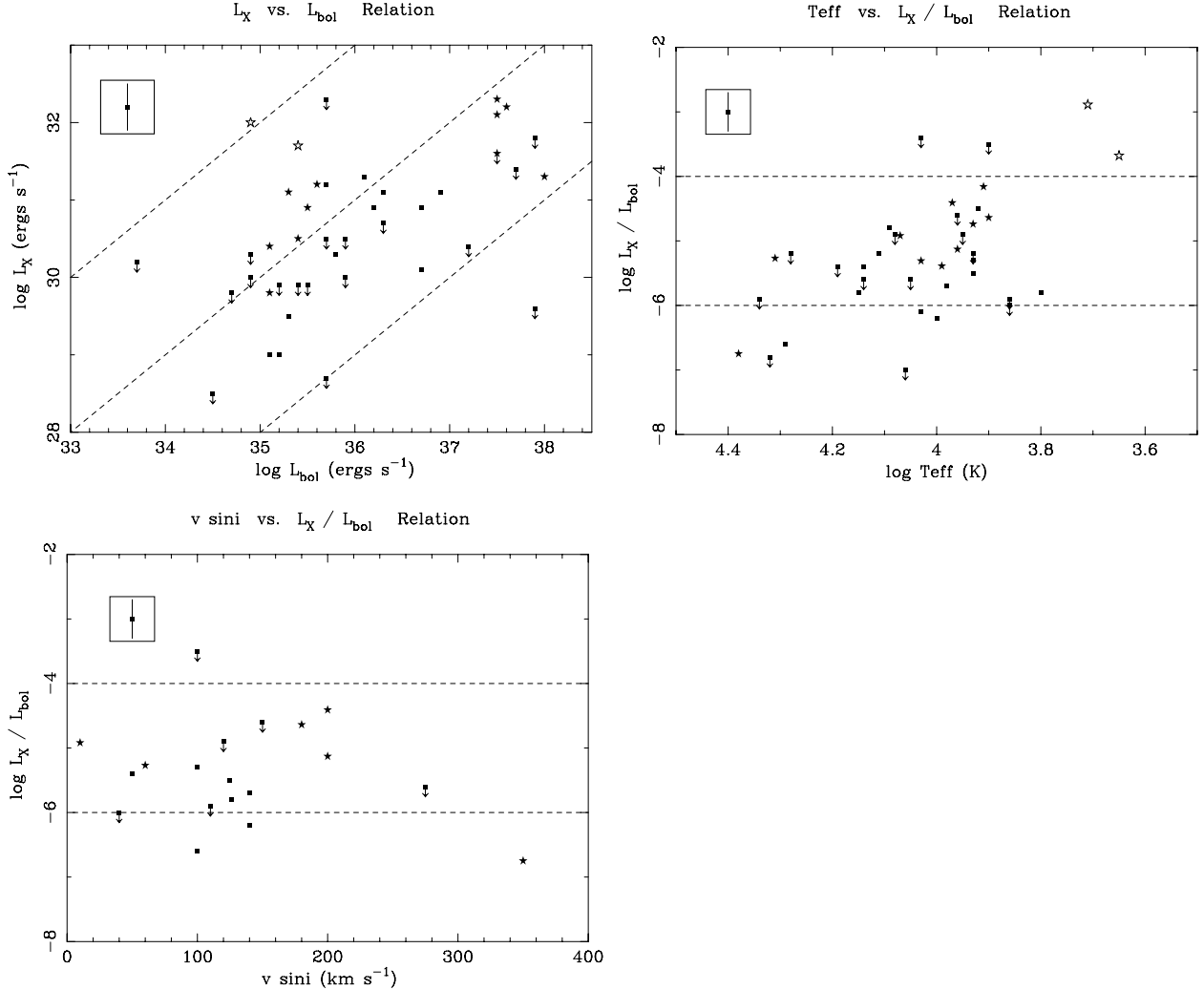


Fig. 13.— a: Log  $L_X$  vs. log  $L_{\text{bol}}$  relation (*top left panel*), b: log  $L_X/L_{\text{bol}}$  vs. log  $T_{\text{eff}}$  relation (*top right panel*), c: log  $L_X/L_{\text{bol}}$  vs.  $v_{\text{rot}} \sin i$  (*bottom left panel*). Filled and open stars represent HAeBes and proto-HAeBes of *ASCA* samples, respectively. Filled squares represent HAeBes of *ROSAT* samples. Points with arrows represent upper-limit.  $L_X$  of *ROSAT* is converted to the *ASCA* band assuming  $kT = 2$  keV, abundance =  $0.3Z_{\odot}$  and  $N_{\text{H}}$  converted from  $A_V$  (Ryter 1996). The plot in the upper left box represents typical error ranges of *ROSAT* samples if  $kT$  changes between 0.5–4 keV. Barred lines in the figure (a) show  $\log L_X/L_{\text{bol}} = -3, -5$  and  $-7$  from the top, respectively.

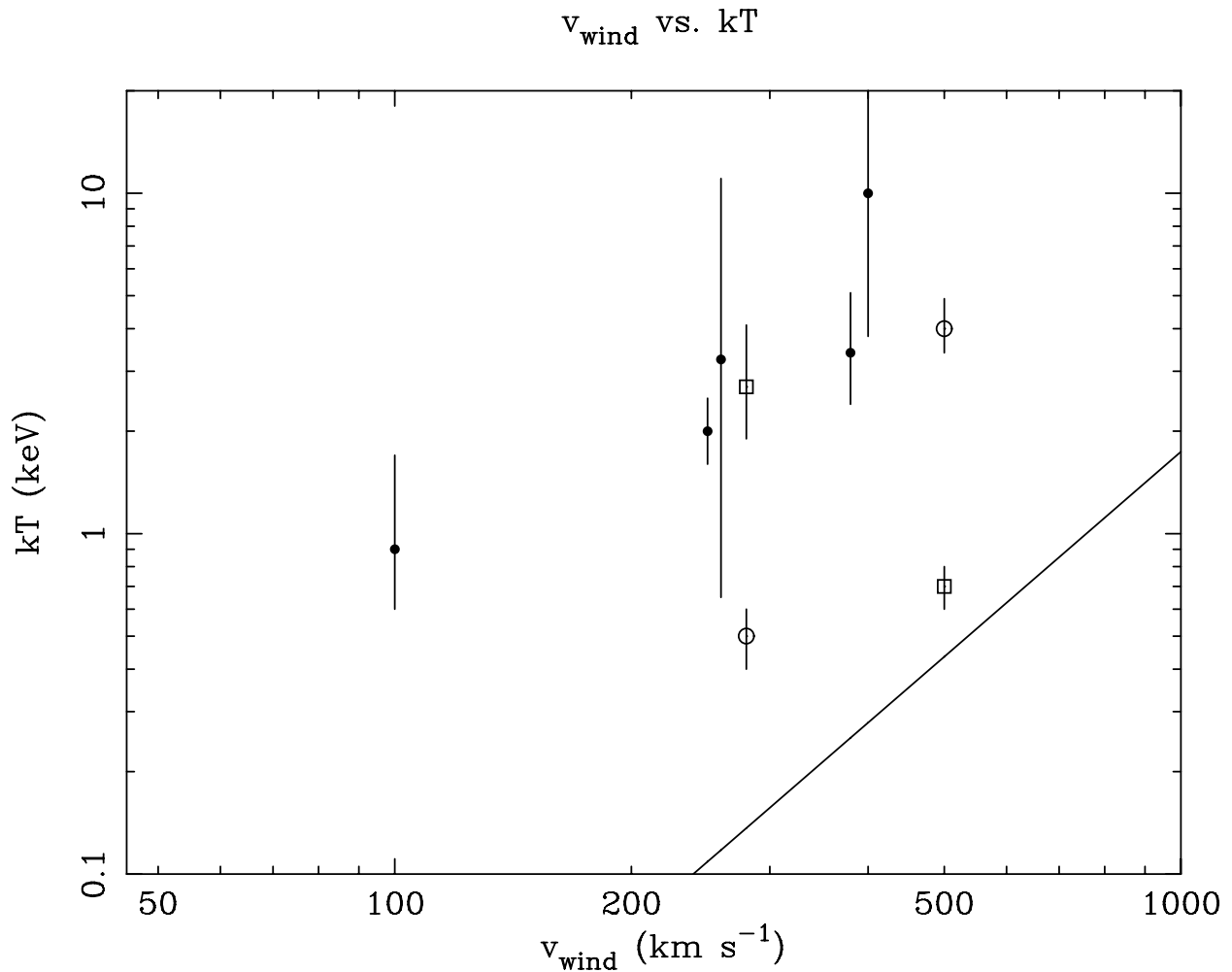


Fig. 14.—  $kT$  vs. terminal velocity of the stellar wind ( $v_{\text{wind}}$ ). Dots are 1T sources. Open circles and squares are dominant (i.e. large  $L_X$ ) and minor (i.e. small  $L_X$ ) components of 2T sources, respectively. The solid line denotes the plasma temperature when whole kinetic energy converts to the thermal energy (i.e.  $3kT=m_p v_{\text{wind}}^2/2$ ,  $m_p$ : proton mass).

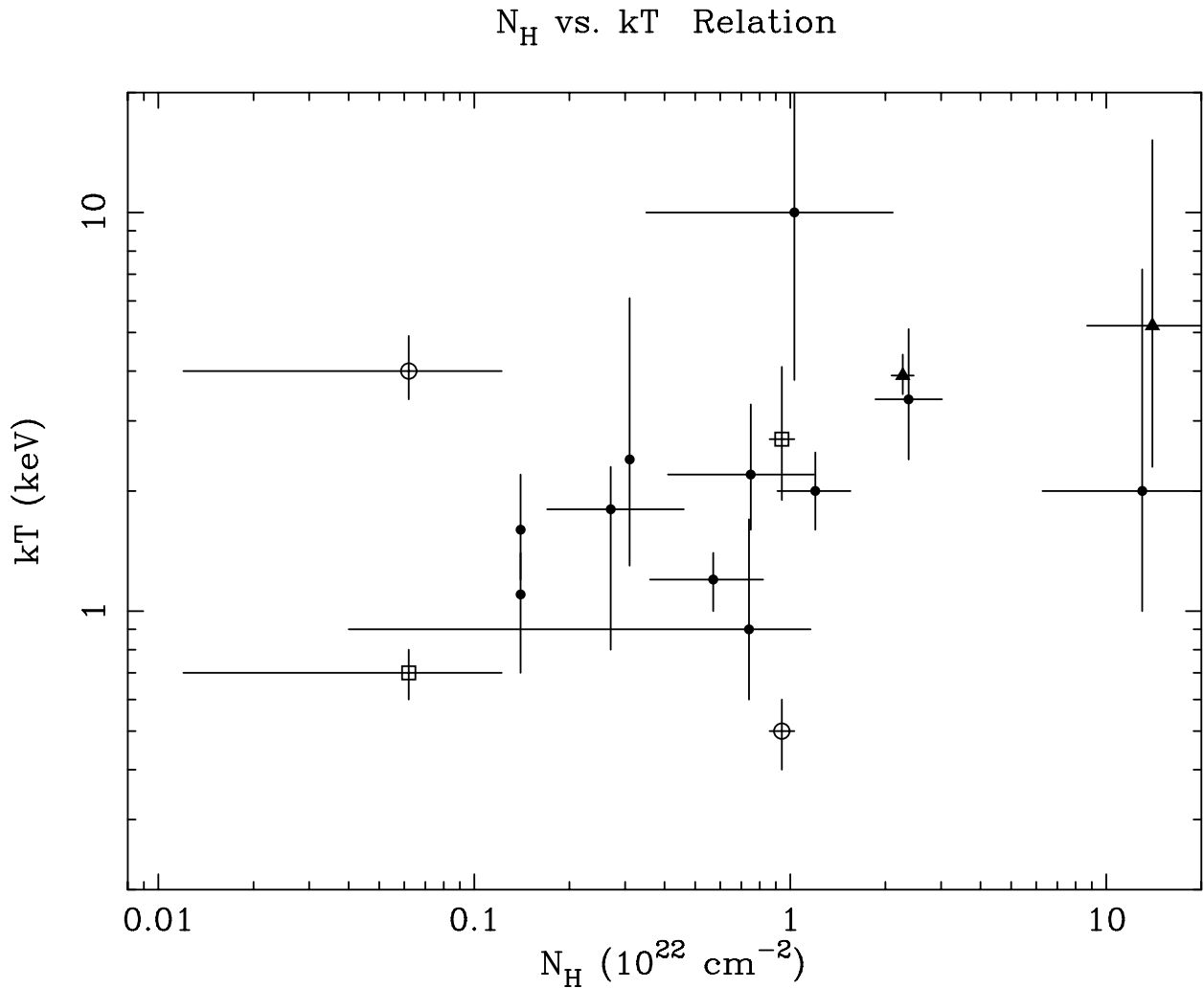


Fig. 15.—  $kT$  dependence on  $N_H$ . Dots, open circles and squares are the same as in Figure 14. Proto-HAeBes (1T) are shown as filled triangles.  $N_H$  less than  $10^{21} \text{ cm}^{-2}$  is referred to the  $A_V$ -converted  $N_H$ .

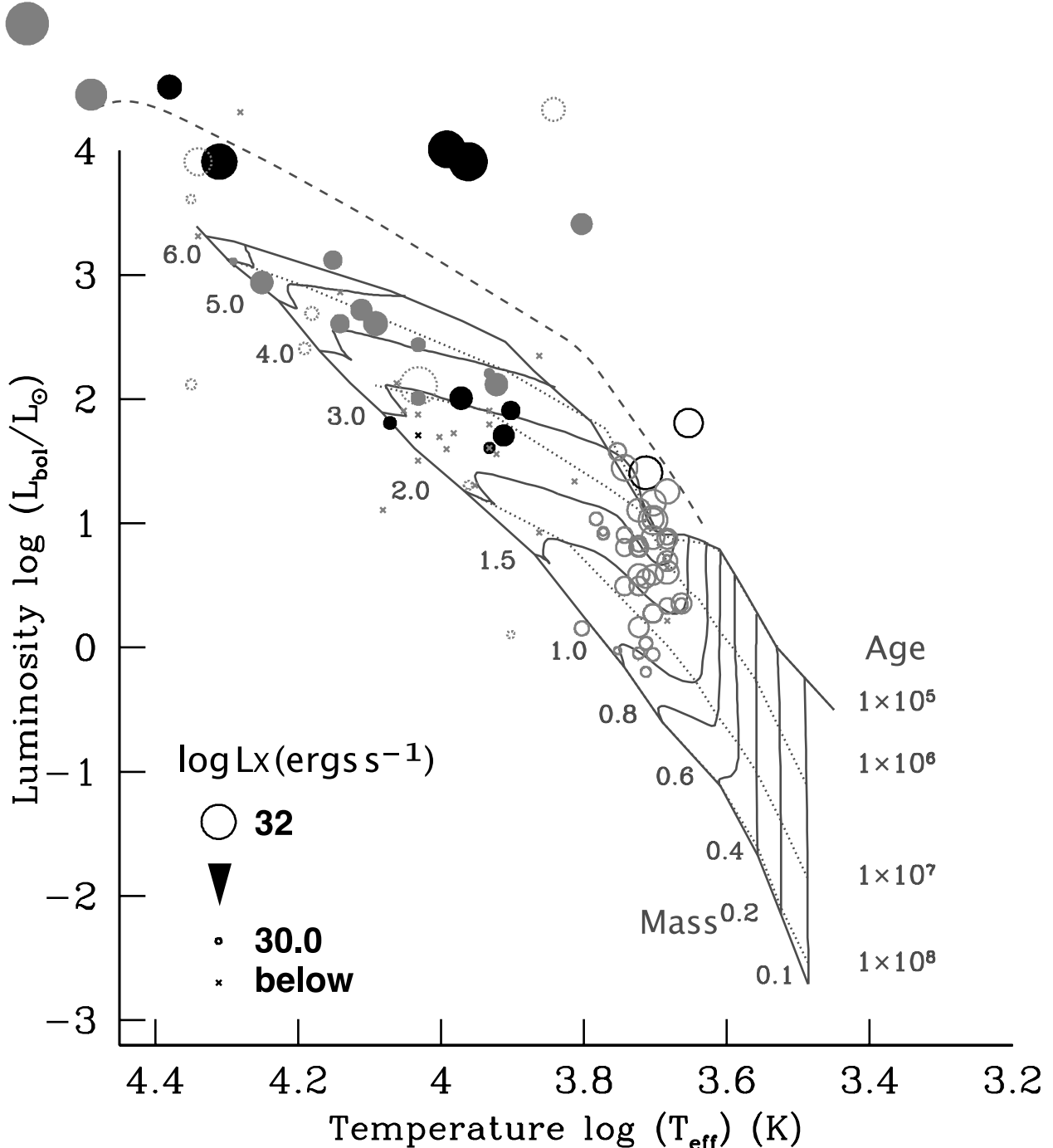


Fig. 16.— X-ray luminosity of young intermediate-mass stars in the HR diagram. Circle size is proportional to  $(\log L_X \text{ ergs s}^{-1} - 30)$  and crosses are  $\log L_X < 30 \text{ ergs s}^{-1}$  (both detected and upper limit sources). Luminosity upper limit on  $\log L_X \geq 30 \text{ ergs s}^{-1}$  is drawn by dotted circles. Black and grey are *ASCA* and *ROSAT* samples, respectively. HAeBes are drawn by filled circles and proto-HAeBe candidates (EC 95 and SVS 63E+W) are two black open circles. Grey open circles and crosses below  $\log T_{\text{eff}} \sim 3.8$  K are sources in the Orion cloud (Gagné et al. 1995) (Undetected sources with upper limit above  $10^{30} \text{ ergs s}^{-1}$  are not included). The diagram is overlaid on a stellar evolutional track modeled by Palla & Stahler (1993). A broken line means the birth line when accretion rate is  $\dot{M} = 10^{-4} M_{\odot} \text{ yr}^{-1}$ .

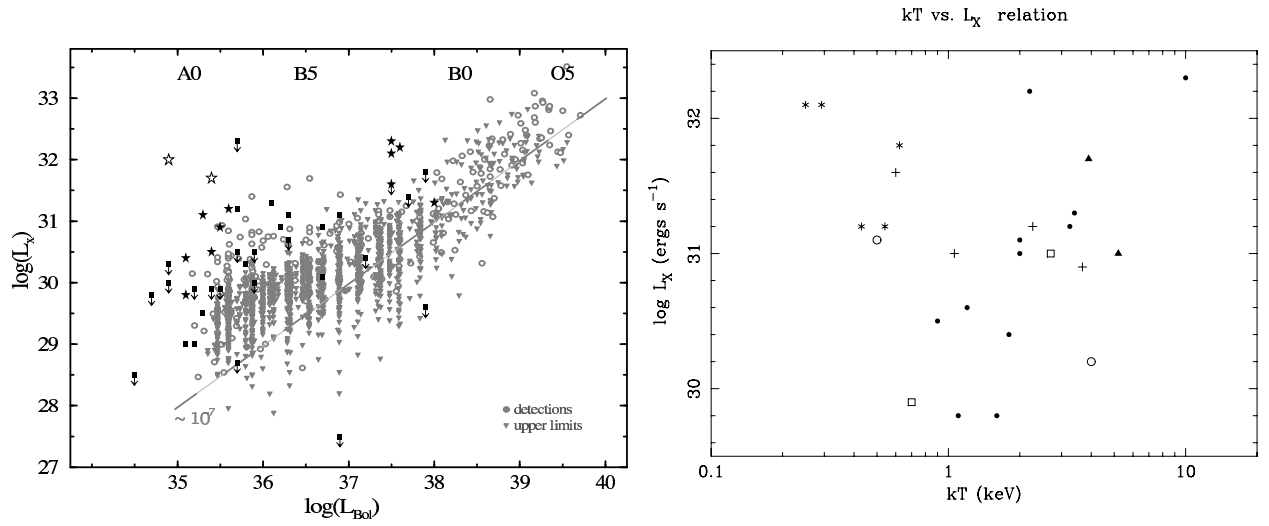


Fig. 17.— a: Log  $L_X$  vs.  $\log L_{\text{bol}}$  relation of HAeBes (black) overlaid on those of MSs (gray, figure 4 in Berghöfer et al. (1997)) (left panel). Marks of HAeBes are the same as those in Figure 13a. b: Log  $L_X$  vs.  $kT$  relation of massive MS stars and HAeBes (right panel). Asterisks are cool components of 2T sources or 1T sources of massive MS stars. Crosses are hard X-ray tails of massive MS stars. Other marks for HAeBes and proto-HAeBes are the same as in Figure 15.